This manuscript is a preprint and has been submitted to *Basin Research*. This manuscript has not undergone peer review. Subsequent versions of this manuscript may have different content. If accepted, the final accepted version of this manuscript will be available via the 'Peer-reviewed Publication' DOI link on the right-hand side of this webpage. Please feel free to contact any of the authors directly to comment on the manuscript. We welcome any feedback!

Subsurface temperature of the northern North Sea Basin

***Arka Dyuti Sarkar*[1,2]**

***Mads Huuse*[1]**

[2]*Corresponding author: arkadyuti.sarkar@manchester.ac.uk*

[1]*Basins Research Group, Department of Earth and Environmental Sciences, University of Manchester, Manchester M13 9PL, United Kingdom*

Acknowledgement

This project was enabled by generous funding from Arka's parents, to whom the authors are very grateful. Thanks go to CGG for provision of the North Viking Graben dataset and to Schlumberger for provision of Petrel licenses (the software used for modelling). Special thanks go to Dr Kofi Owusu for his comments and assistance in modelling remotely during a pandemic. Thanks also go to colleagues at the Basin Research Group for their support and guidance.

Abstract

The North Viking Graben (NVG) is part of the mature North Sea Basin petroleum province and designated as a major carbon storage basin for NW Europe. It has been extensively drilled over five decades with an abundance of well and seismic data in the public domain. As such it serves as an excellent setting to demonstrate the efficacy of a proprietary seismic data led approach to modelling subsurface temperatures using a state-of-the-art full waveform inversion velocity model covering the entire NVG. In a forward modelling problem, an empirical velocity to thermal conductivity transform is used in conjunction with predefined heat flow to predict subsurface temperature. The predefined heat flow parameters are set based on the range of values from previous studies in the area. Abundant well data with bottom hole temperature (BHT) records provide calibration of results. In the inverse modelling problem, BHT's as well as the velocity derived thermal conductivity are used to solve a 1D steady state approximation of Fourier's Law for heat flow. In this way heat flow is interpolated over the 12000 km^2 model area at a km scale (lateral) resolution, highlighting lateral variability in comparison to the traditional point-based heat flow datasets. This heat flow is used to condition a final iterative loop of forward modelling to produce a temperature model that is best representative of the subsurface temperature. Calibration against 139 exploration wells indicate that the predicted temperatures are on average only 0.6 °C warmer than the recorded values, with a root mean squared error range of 5 °C. BHT for the recently completed Northern Lights carbon capture and sequestration (CCS) well 31/5-7 (Eos) has been modelled to be 97 °C, which is within 6 °C of the recorded BHT. This serves to highlight the applicability of this workflow not only towards enhancing petroleum systems modelling work but also for use in the energy transition and for fundamental scientific purposes.

Keywords:

Seismic; velocity modelling; subsurface temperature

1. Introduction

The importance of understanding the subsurface temperature conditions is manifold. An understanding of the isotherms may help delineate important temperature driven diagenetic boundaries (Bjørlykke et al., 1989). Similarly, it is useful for petroleum exploration as it can instruct as to the nature of the hydrocarbons to be expected from a source rock (Allen & Allen, 2013). Unlike frontier areas where the effectiveness of source rocks may be in doubt, this is not a concern in the North Sea. However, understanding of the present-day subsurface temperature can still prove useful in such a mature basin. Analysis of global hydrocarbon resources has shown that there exists a narrow thermal window, the so called “Golden Zone” (Nadeau, 2011), where diagenetic processes for clay minerals for example are conducive to porous reservoirs. Similarly, an improved understanding of subsurface temperature could assist in enhanced oil recovery (EOR) such as when CO_2 saturation is used to aid recovery of heavy oils by reducing the density of the latter (Davarpanah & Mirshekari, 2020). Investigations into geothermal energy also benefit from improved understanding of subsurface temperature conditions (Bonté et al., 2012; Fuchs & Balling, 2016). The North Sea is one of the world’s most prolific and extensively studied petroleum provinces (Copestake et al., 2003; Cornford, 1998; Leadholm et al., 1985; Rüpke et al., 2008). Over the course of the past sixty years numerous oil and gas fields have been discovered, many of which have served as the testing ground for new technologies such as time lapse 4D seismic or EOR (Awan et al., 2006; Landrø et al., 1999). With this history of developing and applying cutting edge methodologies, it is a fitting setting to test the workflow proposed here. This paper proposes and tests a means of utilising seismic data to predict subsurface temperatures. Previous work has demonstrated that a transform based on empirical velocity and thermal conductivity data may be utilised to convert seismic velocities to thermal conductivities (Sarkar, 2020). The derived thermal conductivities may be used in conjunction with heat flow data, either from existing open source data or through modelling of heat flow, to determine subsurface temperatures from Fourier’s Law under a steady state condition. Historically there have been numerous studies of the thermal conductivities and heat flow of sediments in the northern North Sea (Andrews-Speed et al., 1984; Brigaud et al., 1992; Cornelius, 1975; Evans, 1977; Evans & Coleman, 1974; Houbolt & Wells, 1980; Leadholm et al., 1985). However, there seems to be a hiatus in such studies in recent times. As such it is envisioned that the output from the thermal modelling work in this study will add to the existing body of knowledge in that regard. The Northern Lights project is an initiative by the Norwegian government with industry partners to undertake full scale carbon capture and sequestration (CCS) (Cozier, 2019). The injection well 31/5-7 (Eos) appraised the target site in March 2020 and its temperature has been modelled here to demonstrate the efficacy of the proposed methodology.

1.1 Thermal modelling fundamentals

To understand how subsurface temperature might be modelled in the present day it is important to establish the key thermal boundary conditions and properties. These are heat flow, seabed temperature, thermal conductivity, the resultant geothermal gradient and subsurface temperature. The link between heat flow, thermal conductivity and geothermal gradient can be represented by the 1D approximation of Fourier's Law (Eq. 1).

Equation 1: $Q = k \times \frac{dT}{dZ}$

Where Q is heat flow (mW m^{-2}); k is thermal conductivity (W m^{-1} K^{-1}) and dT/dZ is geothermal gradient (°C km^{-1}).

To estimate the temperature below a certain depth in the subsurface, the rate of change of temperature with depth, i.e. the geothermal gradient is the most important parameter. It becomes apparent then that by rearranging Eq. 1, the input parameters necessary to estimate this are heat flow and thermal conductivity.

Equation 2: $\frac{dT}{dZ} = \frac{Q}{k}$

Thermal conductivity is a measure of the ease with which heat may be conducted through a material (Popov et al., 2003) and is thus critical to estimating the thermal structure of the subsurface. Thermal conductivity data from direct measurements are made either in situ through well logs or via direct measurements on recovered samples (Andrews-Speed et al., 1984; Jorand et al., 2015; Schön, 2015a). Measuring tools include either a needle probe inserted into a sample or a divided bar apparatus (Evans, 1977; Horai, 1982). However, these measurements may suffer from issues that affect both their ease of acquisition and reliability. For example thermal conductivity probes may have poor contact with borehole walls, or the needle probe reading might be affected by the alignment of the mineral fabric in relation to the needle orientation (Lucazeau et al., 2004; Pribnow et al., 2000). As a result there has been considerable thought put towards deriving thermal conductivity from other more easily measured physical properties such as bulk density, porosity or compressional sound wave velocity (Boulanouar et al., 2013; Esteban et al., 2015; Gu et al., 2017; Hartmann et al., 2005; Horai, 1982; Jorand et al., 2015). In the case of velocity, it is found to have similar sensitivity to properties as thermal conductivity (Houbolt & Wells, 1980). That is, thermal conductivity is primarily affected by the mineral composition, porosity and presence of fractures (Mielke et al., 2017; Pimienta et al., 2018; Zamora et al., 1993). Temperature and pressure also impact thermal conductivity though not as much as the other factors (Leadholm et al., 1985; Lee, 2003).

Figure 1*: Study area overview*

2. Geological history

The North Viking Graben (Fig. 1, 2) is located in the Northern North Sea between the UK continental shelf (UKCS) to the West and the Norwegian coast to the east, and part of the north western European cratonic block (Brigaud et al., 1992). It is part of the North Sea Graben system, which controlled Cretaceous-Cenozoic subsidence of the basin (Cornford, 1998). It is a Mesozoic rift system, with the rifting in this area having occurred after the Caledonian orogeny (and extensional orogenic collapse), with there being two primary phases of extensional rifting since the Devonian (Fichler et al., 2011; Rüpke et al., 2008; Ziegler, 1992). Primary rifting in the Permian to Early Triassic was followed by a post rift subsidence period (Nøttvedt et al., 1995). The next phase of rifting was from lower to mid Jurassic to early Cretaceous and was also followed by a post rift subsidence period. The rift axis for the Permo-Triassic rifting is believed to be located under the present Horda Platform with the late Jurassic rift axis below the present day Viking Graben (Christiansson et al., 2000). No major tectonic activity is believed to have occurred post Jurassic though there is some conjecture regarding a Tertiary rifting episode (Rüpke et al., 2008) and mid Miocene inversion (Løseth et al., 2013, 2016). The predominant rift direction in the N to NE striking Viking Graben was west-east and northwest-southeast.

Crustal basement rocks in this area have a history exceeding one Wilson cycle and trace back to the junction between the Laurentian and Baltican plates, including the opening of the Iapetus Ocean, island arc development linked to oceanic subduction and the Caledonian orogeny (Fossen et al., 2008; Meert & Torsvik, 2003). The composition of the basement rocks can be seen to vary from granites underneath the East Shetland Platform to low and intermediate grade metamorphic and metamorphosed sediments below the Viking Graben and Horda Platform (Fichler et al., 2011). The sedimentary record in this area is Devonian and younger. Sand and shales dominate the Triassic to Jurassic basin fill with carbonates and shales predominant in the Cretaceous (Brigaud et al., 1992). Tertiary lithologies consist of shales, silts and sands, with a brief period of Paleocene volcanism marked by the widespread deposition of volcanic tuffs across the graben (Haaland et al., 2000).

Source rocks in the area are predominantly Kimmeridge Clay (shales) that were deposited briefly in the Late Jurassic (Davison & Underhill, 2012; Gautier, 2005). Abundant reservoir rocks are available in the NVG (with one such reservoir including the pre rift Lower-Mid Jurassic sandstones) all of which exist with a variety of trapping mechanisms. These pre rift reservoirs are usually found in tilted fault blocks where fine-grained post rift sedimentary sequences act as seals. Commonly in the Viking Graben these vertical seals are unconformably overlying shales.

Figure 2*: Structural transect*

3. Data

The data used for the study can be subdivided into seismic data and borehole data.

The North Viking Graben megasurvey was acquired by CGG between 2014 and 2016, covering a total area of 35410 km^2. This broadband 3D seismic reflection survey of BroadSeis™ and BroadSource™ configuration covers the northern North Sea basin and was shot in a north-south direction, recorded in TWT down to 9 seconds with an acquisition sample interval of 2 ms (Purvis et al., 2018) though for this work the depth converted volume was utilised. It was acquired using 324 & 328 acquisition lines (due to merging of two separate survey areas: Horda and Tampen respectively) with 6.25 x 18.75 m bin spacing and a line separation of 75 m. A (flip flop) shot point interval of 18.75 m and a source separation of 37.5 m gives a nominal common-mid-point (CMP) fold of 106. Twelve streamers were used in total, each 7950 m long, with 636 channels towed at depths of 7 – 50 m (BroadSeis™ profile).

Multiple algorithms were used to remove noise and multiples. Both manual picking and time tomographic inversion (TOMOT) was used to generate velocities with imaging done using Kirchhoff PSTM. A proprietary CGG methodology of continuous automatic bi-spectral velocity picking helped generate the final stacking velocities (Purvis et al., 2018). The processed PSTM and PSDM cubes underpin the modelling work conducted in this study.

The full waveform inversion (FWI) technique aims to produce a high-fidelity subsurface representation of velocity, as the velocity model minimises differences between observed and modelled seismic waveforms within the original raw data (Warner et al., 2013). In making the FWI velocity product, a best guess starting model based on seismic processing velocities is iteratively improved using a sequence of linearized local inversions (Warner et al., 2013). For the CGG NVG survey the fast track velocity product was made from the Dix conversion of root mean squared (RMS) stacking velocities, followed by Kirchhoff depth migration to residual move out (RMO) velocities (CGG, 2019). By starting at low seismic frequencies with the tomography process for the FWI model build, the risk of cycle skipping was minimised (CGG, 2019). During the FWI process, the model was subdivided into smaller areas targeting regions of key geology, allowing verification to be conducted (CGG, 2019). Three production runs at ever increasing seismic frequency (4; 5.5 & 8 Hz) were conducted as part of the FWI model build (CGG, 2019). The final 8 Hz update produced the velocity model that best follows geological structure and can characterise small scale features such as injectites (CGG, 2019). The FWI model was calibrated using 101 wells with QC checks completed against sonic log data (CGG, 2019).

Borehole data for this study were primarily sourced from the Norwegian Petroleum Directorate (NPD) website. This gave access to well reports, mud logs, geological reports, and wireline logging data. Because the FWI volume was already calibrated against downhole sonic velocity data and provided in the depth domain, the primary data of interest for this study were the bottom hole temperatures (BHT) recorded for each well within the thermal model area. Publicly available heat flow data from the International Heat Flow Commission database were used to provide constraint on the heat flow parameter (Gosnold & Panda, 2002). There is a scarcity of data points covering the model area as seen in Fig. 4 with the nearest offshore data point too distant to confidently interpolate from (Ritter et al., 2004). In the absence of suitable heat flow control a combination of published heat flow estimates from various authors has been used (Fig. 4) (Davies & Davies, 2010; Davies, 2013; Lucazeau, 2019).

Figure 3*: Seismic velocities (interval and average)*

Figure 4*: Heat flow data in context of study area*

4. Methods

The modelling work has been conducted using Schlumberger's Petrel software suite, with it being used for 3D seismic interpretation over the extent of the survey as well as to create and manipulate the property volumes and thermal models in this work. Standard seismic interpretation techniques, including horizon mapping, surface map creation and seismic attribute extractions were conducted for a structural interpretation of two reference horizons, the seafloor and the Base Cretaceous Unconformity (BCU) (Cox et al., 2020; Posamentier, 2004). The BCU follows the regional stratigraphic framework and serves as a reference horizon, upon which model outputs are overlain as attributes, thus giving a regional context to the results (Evans, 2003). The seafloor is the ceiling for the thermal models, separating the hydrothermal and the geothermal domains. Both horizons were mapped in depth using the 3D reflection seismic data. The bathymetry was ground truthed with the open source bathymetric grid data from GEBCO (Becker et al., 2009). For the purposes of this work, no other structural interpretation was necessary. Further interpretation or import of grids can of course be done to observe the predicted temperature at desired stratigraphic levels.

The workflow utilised in this project is summarised in Fig. 5. It can be broken down into two main problems: the forward modelling problem uses the seismic velocity data as the input parameter to model for thermal conductivity and subsurface temperature using constant heat flows, which in turn is calibrated against available BHT data; the inverse problem calculates heat flow from the observed BHTs and the average thermal conductivity volume. As heat flow is an important input parameter to model temperature, it becomes possible to update the temperature forward model with the inverse modelling results, and thus validate the final temperature model results, in a manner akin to tomographic update of velocity models (Jones, 2018; Prada et al., 2019).

***Figure 5**: Reflection seismic thermometry workflow*

4.1 Forward modelling problem – present day subsurface temperature

The seismic dataset was a modern broadband seismic survey covering the North Viking Graben (NVG) spanning across parts of the UK and Norwegian continental shelves (UKCS and NCS, respectively). The full waveform inversion (FWI) final velocity model is the key seismic data product underpinning the modelling work.

4.1.1 Thermal conductivity structure

This study uses a high-resolution 3D seismic velocity volume and experimental data relating velocity and conductivity with an empirical relationship (Fig. 6). As this project outlines a remote sensing method, direct thermal conductivity measurement is not possible and instead it must be indirectly determined. If the rocks of the subsurface are considered as a multi component system comprised of minerals, texture (of grains, such as their shape and size), porosity and the fluid content, it becomes possible in an ideal scenario to determine the composite effective thermal conductivity from the contribution of each component part using a suitable mixing law or effective medium model (Duffaut et al., 2018; Hartmann et al., 2005; Schön, 2015b). In the presented scenario, it is not possible to determine the volumetric fraction of each mineral for example as can be normally done from logging data (Brigaud et al., 1990). The elastic properties of the subsurface are well constrained from seismic data (Mavko et al., 2009) and it provides the avenue to the desired thermal structure. To link thermal properties (thermal conductivity) to elastic properties (acoustic velocity), knowledge of their primary controls becomes necessary. Experimental work has shown that these controls include mineral composition, texture, porosity, the presence of fractures and fluid fill (Gegenhuber & Schoen, 2012). It helps to think of porosity as the crucial intermediary in the proposed empirical relationship as there have been studies examining the link between acoustic velocity and porosity (Eberhart-Phillips et al., 1989; Lee, 2003; Velde, 1996); and similarly the relationship between porosity and thermal conductivity (Fuchs & Förster, 2013; Jorand et al., 2015). By making the direct leap it must be noted that there are inherent assumptions in such an approach. One concern that may arise is the extent to which the variation in the velocity signal solely corresponding to a thermal conductivity variation (as desired) or is it in fact influenced by external factors (for example fluid overpressure). In such an instance, this issue may be obviated by restricting application to regions of hydrostatic fluid pressure only, however it might be the case that slight overpressure would only correspond to a minor increase in velocity (Lee, 2003). It must be noted that even the best thermal conductivity models are subject to caveats, either in the form of the inherent assumptions or the specific circumstances where direct relationships might not be as strong.

By including a wide range of studies, covering a wide array of lithologies and settings, it is hoped that the resulting empirical relationship can serve as a robust first order estimate for the varying porosities encountered within the study area. The sample dataset is limited to wet samples only and measurements taken using transient measurement apparatus such as the optical scanning method (Popov et al., 1999), in order to maintain applicability to fluid filled rocks in the subsurface and parity between data points respectively. This approach has previously been applied in passive margin settings offshore Namibia and offshore USA (Sarkar & Huuse, 2018). The best fit regression through the subset of points is as follows:

Equation 3: $k_V = (6 \times 10^{-5}) {V_p}^{1.3279}$

Where k_V is thermal conductivity from velocity (W m^{-1} K^{-1}) and V_P is P wave velocity (m s^{-1})

Figure 6*: Empirical transform for velocity and thermal conductivity*

With a highly detailed FWI velocity volume representing the P-wave velocity of the subsurface and a function relating velocity and thermal conductivity, it is possible to convert the FWI velocity volume into a volume of thermal conductivity varying with depth (using Eq. 3). To facilitate the workflow the FWI interval velocity volume was first converted to an average velocity volume in depth below the seabed (as the geotherm starts at seabed) (Fig. 3b) and this in turn allowed the estimation of average thermal conductivity as a function of depth in the entire volume (Fig. 7b).

4.1.2 Heat flow input scenarios

In order to convert the average thermal conductivity (Eq. 2), information regarding the heat flow in the study area is required to determine the geothermal gradient. Initial heat flow values were defined based on the nearest points in the International Heat Flow Database. As seen on Fig. 4, there is a paucity of data points in the study area. This leads to examining the published record for maps of heat flow covering the North Sea, and these tend to exist in the form of heat flow estimate grids at regional or global scale. Examining these grids such as Davies (2013) or Lucazeau (2019), it becomes apparent that the heat flow varies greatly. This seems to depend not just on the size of the grid squares over which the authors have applied their interpolation, but the exact technique used to interpolate and the input parameters they have used will lead to this variability. Consequently it was decided that analysis of the range of heat flow values that are observed in the literature for this area will be used to define predetermined starting conditions for heat flow (Andrews-Speed et al., 1984; Cornelius, 1975; Davies, 2013; Evans & Coleman, 1974; Harper, 1971; Leadholm et al., 1985; Lucazeau, 2019; Ritter et al., 2004). This gives a low-, mid- and high- case heat flow of 60, 70 and 80 mW m^{-2} respectively.

4.1.3 Temperature grids & calibration

Having determined thermal conductivity and established heat flow scenarios it becomes possible to calculate three geothermal gradient scenarios for the model area. By convolving this with the subsurface depth and incorporating the bottom water temperature (BWT) (i.e. seabed temperature) an estimate of present-day subsurface temperature can be made.

Equation 4: $T = T_{SEABED} + (\frac{dT}{dZ} \times Z_{SUBSURFACE})$

where *T* is predicted temperature (°C); T_{SEABED} is the temperature at seabed (°C); *dT/dZ* is the instantaneous geothermal gradient (°C km^{-1}) (Eq. 2); and $Z_{SUBSURFACE}$ is the subsurface depth (km).

Early studies into the geothermal aspects of the North Sea would set temperature at the seafloor to a constant, for example 10 °C (Cornelius, 1975; Evans & Coleman, 1974; Harper, 1971). Here however seafloor temperature was assigned through decadal averages from the World Ocean Atlas (WOA) dataset (Boyer et al., 2014; Locarnini et al., 2013). Using the nearest measurement node from the 0.25-degree grid of the WOA dataset, the temperature profile (hydrothermal gradient) for this was used to interpolate seafloor temperatures across the seafloor depth grid. By basing the seafloor temperatures on a decadal average, the variability of seasonal bottom water conditions and longer scale variability will be negated, thus giving a baseline temperature from which the well readings can be seen in context to, particularly with regard to determining the geothermal gradient.

Thermograms, or temperature profiles, depicting temperature change with depth are one way of displaying the model results for each well site (Cornelius, 1975). Petrel allows for the creation of synthetic logs from a reservoir model or pillar grid. This requires resampling the temperature models into a pillar grid coincident with the extent of the area of interest.

Resampling of the seismic attribute volumes was done using the interpolation algorithm. The dimensions of the individual cells of the grid, and subsequently the total number of cells constituting the entire grid are important with respect to the total compute power. The modelling results displayed here have a lateral resolution of 50*50 m (XY orientation), with the top of the model coinciding with mean sea level (MSL) and the base being set at 5.5 km depth. This basal depth encompasses the maximum vertical depth of the wells used for calibration. Cell height was set to 20 m, in accordance with the vertical resolution of the velocity data. For these dimensions, the entire gridded model comprises about 1.4 billion voxels.

With all the input and derived seismic attributes resampled as properties in the pillar grid, synthetic logs for each well are generated. These synthetic logs are made for the three temperature prediction volumes coincident with the three heat flow input scenarios. The estimated temperature at the bottom of each well from the synthetic logs is then plotted against the recorded corrected BHT. Theoretically, the misfit between observed and modelled temperature for each well can be used to calculate how much the heat flow input for each well must be adjusted for there to be no misfit. In this way, the most representative heat flow value for the area might be calibrated.

4.2 Inverse modelling problem – solving for heat flow

The first stage of subsurface temperature modelling assumed 3 discrete heat flow scenarios. In this instance, discrete values for heat flow across the model area was used to simulate each temperature scenario. However, heat flow is likely not homogeneous across the model area and there may be lateral variability across individual structures and preferred fluid migration paths. If recorded temperatures in the wells are assumed to be correct and with knowledge of the seafloor temperature, geothermal gradient can be independently computed for each well site. Additionally, if the seismic velocity derived thermal conductivity is considered valid, it becomes possible to use the 1D approximation of Fourier's Law to derive heat flow at each well location. This is the inverse problem.

Equation 5: $Q = K_V \times \left(\frac{T_{BHT} - T_{SEAFLOOR}}{Z_{TVD}}\right)$

Where Q is heat flow (mW m^{-2}); K_V is thermal conductivity from velocity (W m^{-1} K^{-1}); T_{BHT} is bottom hole temperature (°C); $T_{SEAFLOOR}$ is temperature at seafloor (°C); and Z_{TVD} is true vertical depth for hole bottom (km).

It must be noted that some wells are deviated and thus care must be taken not to use total depth or measured depth when computing the geothermal gradient from BHT. Instead the true vertical depth (TVD) is used with the coordinates of the hole bottom being assigned as the surface location for a pseudo well head. This is done in order to ascertain the seafloor temperature vertically above the hole bottom, thereby obviating the introduction of a lateral BWT variability element to the computation.

Interpolating for heat flow between the wells creates a map of inversely modelled laterally varying heat flow. An inverse distance weighting (IDW) function has been used to interpolate (on both ArcPro and Petrel for cross verification). The values of cells in the vicinity of the processing cell (interpolated gap) are averaged, with the distance of the neighbouring cell having an inverse weighting (Watson & Philip, 1985). Though kriging is a more advanced geostatistical procedure, it is more time consuming and thus was not pursued for this first order estimation of heat flow.

4.3 Final temperature model

Calibrating the results of the temperature forward model with the different heat flow input scenarios, it is likely to show different degrees of agreement. Iteratively updating the heat flow input each time and remodelling for subsurface temperature should theoretically permit the most representative heat flow across the study area to be arrived at ultimately. However, this former approach was not pursued as it was shown previously that inverse modelling allows the determination of laterally varying heat flow across the model area. Convolving this heat flow with the seismically derived thermal conductivity (Eq. 2), it should be possible to generate a volume of instantaneous geothermal gradient that has most agreement across all the calibration wells. This thermal gradient is used to generate a final temperature model (Eq. 4) that is resampled into the pillar grid and used to output synthetic temperature logs. Predicted temperature from these logs at hole bottom is extracted and used to calibrate against recorded BHT as before.

The well 31/5-7 is located due south west of Troll A field and targets the lower Jurassic Cook and Johanssen formations for injection. The targeted interval has ca.173 m of sandstone overlain by 75 m of shale acting as a seal above it. Pressure data indicates no communication in rocks above and below the shale, reinforcing its seal properties. With no results from this well published due to its very recent completion, it was decided to use the available details (well head coordinates and total depth) to simulate the temperature profile for this well using our model.

5. Results

The results from the modelling work are presented either as seismic attribute overlays on transects or by means of attribute maps on a gridded horizon. But for the purposes of calibration the primary output is the synthetic temperature log data from the wells. These results are discussed individually in the following section.

The FWI interval velocity volume was converted to an average velocity volume (Fig. 3), before applying the velocity to thermal conductivity transform (Fig. 6) to produce a volume of average thermal conductivity (Fig. 7b). Looking at the internal velocity derived thermal conductivity structure (Fig. 7a), the direct nature of the bulk shift results in the thermal conductivity variation with depth across the volume corresponding to the level of detail seen in the input velocity (Fig. 3). When conversion is based on the average velocities, thermal conductivity is seen to vary much more smoothly across the depth interval displayed, as expected (Fig. 7b). Cretaceous and younger Cenozoic sediment cover is seen to have relatively low thermal conductivities, with a distinct increase in thermal conductivity seen in the tilted fault blocks of the Viking Graben. The graben corresponds with the greatest amount of overlying sediment cover and lower conductivities relative to the neighbouring rift shoulder.

Figure 7*: Derived thermal conductivity structure*

The forward modelling results using the predefined heat flow input scenarios are displayed on the west-east transect A-A' (see Fig. 8). As expected, temperatures increase gradually with depth, with no major anomalous zones seen. Cenozoic sediments are coolest with the highest temperatures in the graben itself, which makes sense considering relatively even heat flow but lower conductivities of the sediments within the graben. Isotherms are more widely spaced as we move towards the Horda Platform in the east where the conductivity is greater (Fig. 7). Comparing the results from each heat flow scenario against each other, the broad trend is that increasing heat flow has a directly proportional effect of increasing the recorded temperature at each bottom hole depth. Thus, the greatest range in the predicted temperatures is observed in the high case heat flow model (using 80 mW m^{-2}) (Fig. 8c).

Correspondingly the narrowest range is observed with the low case heat flow model (Fig. 8a). The direct impact of each heat flow input scenario is better visualised when cross plotting the temperature extracted from each well (Fig. 9).

Figure 8*: Forward modelling output for initial heat flow scenarios*

As stated earlier, synthetic thermograms corresponding to the well path of each calibration well was extracted from the predicted temperature models. The temperature at bottom hole in each case has been plotted against the recorded BHT. The best fit regression through each cluster of points and the gradient of this is used as a measure of the degree of agreement between predicted and observed values. The chi-squared value, a measure of statistical validity for each regression line, for all three heat flow scenarios is above the 0.7 that is regarded as being the threshold for statistical reliability. Analysing the misfit between predicted BHT and measured BHT, it is found that on average the low heat flow scenario is 0.64 °C cooler; the mid heat flow scenario has average misfit 15.4 °C higher and the high heat flow scenario has an average misfit of 31.3 °C higher. With increasing heat flow, the corresponding gradient of the regression line through that cluster of points also increases, as does the Y-intercept. The optimum desired gradient that would be expected for best agreement between predicted and observed temperatures would verge on 1, and from this initial forward modelling it is seen that the highest heat flow scenario is closest to this. However, it is also the case that the optimum regression should be seen to pass through the origin of the cross plot and increasing the heat flow moves each regression further away from this.

Figure 9*: Initial forward modelling results calibrated*

Deriving heat flow across the model area (Fig. 10), gives mean heat flow of 60.05 mW m^{-2} and a median of 62.82 mW m^{-2}. The effective range of heat flow is between 40 & 70 mW m^{-2}.

Observing the heat flow variation across the area (Fig 10a) certain wells are seen to have much lower heat flow than their immediate vicinity. Consequently, during interpolation, these wells are seen in a bulls-eye zone of depressed heat flow. The most prominent of these is observed to the south west, with two wells (30/5-1 & 30/8-2) having depressed heat flow. Referring to Fig. 1 these two wells do not coincide with any field. The other prominent heat flow depression is found to the northeast of the model area at the intersection between Troll-A and Troll-B. The north-westernmost and easternmost wells (29/3-1 & 32/4-1, respectively) (Fig. 10a) influence the immediate vicinity by elevating the heat flow interpolated here.

Figure 10*: Inverse modelling of heat flow and results*

The result of running a final iteration of forward modelling for temperature with the continually laterally varying heat flow derived in Fig. 10 is shown in Fig. 11. We find when cross plotting predicted temperatures from this final model against BHT that the general distribution of points has a far tighter spread than in the previous modelling instances. The average misfit between predicted BHT and measured BHT is 0.58 °C. Furthermore, the best fit regression through this set of points has a gradient nearly equal to 1, and passes nearest to the origin, as is expected for the model best reflecting the actual subsurface temperature. Interestingly, the average of the inverse modelled heat flow as stated earlier is nearly equal to the low case heat flow input scenario used in the early stage forward modelling. Looking at the distribution of well points (Fig. 11) however it is clear that there is a great disparity in the two approaches. The visual impact of the two approaches is shown in Fig. 12d, e.

Figure 11*: Well calibration including final temperature model*

The result from the final iteration of the temperature model overlain with key structures is shown in Fig. 12a. Running an RMS amplitude extraction for thermal conductivity on a reference horizon (Fig. 12c), in this case the BCU, it is observed that the highest thermal conductivities are observed in the heart of the Viking Graben, where the BCU is deepest (Fig. 12b). On the flanks of the graben and eastward towards the Horda Platform, thermal conductivities are seen to decrease considerably, consistent with the increasingly shallowing BCU surface at that point. Reverting to the temperature model outputs, we see the difference between the initial forward modelling approach (Fig. 12d) and the final inverse modelled heat flow influenced iteration (Fig. 12e). Comparing the temperatures, within the deep graben for example, it is immediately apparent there is greater variation and detail discernible in from this latter approach. Indeed, what is seen is that some anomalous temperature zones are seen in this final iteration at the northern tip of the Troll field that seem to directly correlate with the anomalous heat flow zone from the interpolation (see Fig. 10a).

Figure 12*: Temperature modelling results*

The results of simulating the thermal profile for the Northern Lights well 31/5-7 (Eos) are shown in Fig. 13, with temperature at bottom hole of 97 °C falling well within the projected 100 °C range published on the project website (see: https://northernlightsccs.com/en/about accessed at 25/07/2020). Data released by Equinor and the Norwegian government in October 2020 with preliminary results indicated temperature at the bottom of 103 °C. The final well report with its BHT record has not yet been made public but preliminary results from the 31/5-7 prediction show a good agreement between model prediction and reality.

Figure 13*: CCS well 31/5-7 modelled*

6. Discussion

There are multiple corollaries of modelling for subsurface temperature in this manner. The seismic led method of deriving subsurface thermal conductivity structure should enable the verification of zones of thermal blanketing (Cercone & Pollack, 1991; Wangen, 1995). Due to the direct relationship between velocity and thermal conductivity as used here, any zones of anomalously high or low velocity will be reflected in thermal conductivity anomalies. However, lithologies that deviate from our general trend (which includes sandstone, shale, limestone and crystalline rocks), such as halite will need to be considered explicitly to represent the temperature above, within and below such anomalous bodies.

The benefit of the highly detailed FWI velocity model available in this area is that the velocity data has been calibrated against wells in the NVG, thus ensuring the velocity model is a good representation of true subsurface properties and conditions. The conversion to thermal conductivity and temperature provides another means of visualising the subsurface. It is of critical importance to both petroleum exploration and carbon sequestration in the area. In other locations such estimates would be highly beneficial to geothermal or gas storage operations. It must be noted that any artefacts in the velocity data will be translated to the derived thermal conductivity, instantaneous geothermal gradient and predicted temperature volumes as a consequence of the direct transitions in the workflow.

6.1 Heat flow modelling – impact and implications

The validation of the inverse modelling of heat flow as an input as opposed to the use of a discrete integer value heat flow input is borne out by the results. The interpolation of heat flow over the 12000 km^2 model area (Fig. 10a) highlights the variation in heat flow magnitude laterally at a much higher resolution than most existing studies. As shown earlier (Fig. 4), global and regional compilations usually produce heat flow grids that are at the scale of 1-degree grid squares or larger. The lateral resolution is thus many orders of magnitude poorer than when based on BHT and conductivity data. Interpolating heat flow at such fine scale might enable the examination of any trends, if any, in heat flow versus features that may be hydrocarbon fields, or structural trends (for example major fault networks). While there is a paucity of data points in the International Heat Flow Database coinciding with large parts of the Northern and Central North Sea, the many decades of hydrocarbon exploration in the area led to numerous wells, many of which have detailed records of BHT. When combined with the seismic velocity driven model to ascertain thermal conductivity structure, it should allow for the possibility to fill in the large gaps in the global point heat flow database, which in turn should allow for more detailed basin scale heat flow studies.

The thermal anomaly visible in the interpolated heat flow map (Fig. 10a) can be seen to coincide with the Troll Field (Fig. 1). Records of this thermal anomaly attribute it to transient effects of uplift caused by late Quaternary deglaciation (Cornford, 1998). The method used to interpolate heat flow might have an impact. IDW gives the best results when the sampling is sufficiently dense with respect to the local variation being simulated (Watson & Philip, 1985). Where sampling is sparse or uneven, the interpolated result will insufficiently represent the desired surface (Philip & Watson, 1982). From the density of wells around existing fields in the area, we can be sure that the IDW interpolation will reliably capture the laterally varying heat flow at this local scale. Nonetheless at the edges of the model area there will be some degree of uncertainty associated with the interpolated heat flow, a consequence of the sampling sparseness in these regions. Kriging would be a more statistically rigorous method of interpolating heat flow, but it requires a prior investigation of the spatial behaviour of heat flow in the sample points. This is incumbent on a pre-existing understanding of the factors influencing the modelled parameter. In a blind test the latter would not necessarily be possible, and thus IDW should be satisfactory for a first order interpretation.

While heat flow has been derived from inverse modelling, in sedimentary basins there is a thermal contribution linked to the radiogenic heat production of sediments and crustal material, and the contribution of heat from the earth's deep interior (that is mantle) (Allen & Allen, 2013; Hasterok et al., 2011; Hasterok, 2010; Hokstad et al., 2017). The modelling here estimated present-day subsurface temperatures using a steady state approximation (Eq. 1). As such, a conscious decision was made to introduce as few variables as possible. Radiogenic heat production would be one such variable. Its impact here has been noted but not explicitly modelled. Mantle heat production is usually estimated from the Moho, whose depth in the area averages roughly 30 km (Grad & Tiira, 2009). Estimates of the Curie isotherm at its shallowest in the study area place it at similar average depths of ca.30 km (Fichler et al., 2011; Kubala et al., 2003). Under the graben, Moho depth does become shallow, up to 22 km in places (Licciardi et al., 2020). Referring to Fig. 10a, modelled heat flow is higher towards the graben centre, which suggests some correlation. With the thermal model base set at 5.5 km, and the degree of shallowing of the Moho not exceeding ~22 km at its shallowest point, the impact of mantle heat input from a modelling perspective is considered negligible in this instance. The general Moho trend in the northern North Sea has a gradual shallowing in the north-west, near the Shetland Islands (Licciardi et al., 2020). If conducting thermal modelling over the whole NVG survey area, and with the basal limits for the model set sufficiently deep such that there might be a basal mantle heat flow effect due to proximity to the Moho for the deepest section of the model.

6.2 Relevance

The applications of this newly validated workflow range from immediate usage by the hydrocarbon industry to supporting new subsurface uses aligned with the energy transition.

Hydrocarbon explorationists may use the knowledge of the isotherms to help develop their petroleum systems models or it can help production teams better ascertain the distribution of temperature in the reservoir in order to inform reservoir engineering projects to maximise recovery. Knowledge of subsurface thermal structure is important for the nuclear waste disposal industry due to the sensitivity of the waste to thermal perturbations (Brigaud et al., 1992). From a low carbon technology solutions perspective, mapping subsurface isotherms may enable geothermal energy prospecting and the understanding of subsurface temperature will be important for CCS operations in both frontier and mature basins.

Simulating temperatures for the current CCS Northern Lights well 31/5-7 emphasises the real-world applicability of this model, both in terms of its speed of producing an estimate and its relevance in the energy transition for the future. It is important to understand the temperature conditions in CO_2 storage reservoirs as the properties of the gas vary with temperature and pressure. Of these only the pressure is routinely estimated based on seismic data (Eiken et al., 2011). At higher temperatures the density of CO_2 decreases, theoretically allowing for a greater volume of it to be stored in a reservoir. Studies of CO_2 injection into the Utsira formation (part of the Sleipnir Project) have shown that reservoir temperature is a source of uncertainty as it can also impact the diffusivity of the gas within the reservoir (Chadwick et al., 2006). By using the subsurface thermal model proposed here, this key uncertainty may be constrained by project planners, both giving more constraint on the volume of CO_2 able to be sequestered within a reservoir, but also the ability to ascertain lateral temperature variability would enable more nuanced storage across different parts of a reservoir. Finally understanding the temperature conditions and where the potential of CO_2 diffusivity is highest could help mitigate the possibility of CO_2 leakage.

It is not just industrial applications for which this methodology may be utilised. Academic end use cases are also envisioned. The study of the microorganisms endemic to the deep subsurface is nascent and opens up the possibility of the crust playing host to potentially great biodiversity and biomass (Basso et al., 2005). Limited studies into the microbial organisms found in oil reservoirs have yielded surprising results. One such study in the Troll field, examining the microbial diversity of produced water, indicated that these microbes were not introduced as contaminants into the reservoir as a by-product of drilling; instead RNA analyses and gene matching has indicated that these are a distinct genera of temperature sensitive microbes that do not match existing known mesophiles or thermophiles (Dahle et al., 2008). Due to the temperature dependence of these novel microbes, and the difficulty with sampling, an understanding of subsurface conditions might help in providing some inclination of the exact genera that can be encountered in a reservoir based on the predicted temperatures from the model. Thus, it is envisioned that the proposed model can assist the microbiological community as well. Bacterial remediation has been studied as a means of clean up for chemical or hydrocarbon contaminated reservoirs or aquifers (Hazen, 1997). Understanding of the temperature field in the subsurface can help determine how conducive the conditions are to the proliferation of such organisms. From a resource perspective microorganisms have been found to impact natural gas, carbon sequestration, hydrocarbons or even interfere with the underground storage of nuclear waste (Christofi & Philip, 1997).

7. Conclusion

The work outlines a novel methodology that utilises state of the art velocity model data from a mature basin such as the North Viking Graben to determine present day subsurface temperatures non-invasively. Forward modelling simulations underpinned by the velocity data and utilising an empirical thermal conductivity transform have been calibrated against recorded temperature data from oil field wells in this sector of the North Sea. Existing work using well data allows the computing of the vertical component of heat flow, in the same orientation as the well. Through inverse modelling here it has been demonstrated that multi axis computing of heat flow is possible with the lateral heat flow variability shown at much higher resolution than existing heat flow datasets. Using this derived heat flow to iteratively update the forward model produced a temperature model, the calibration results for which indicate the validity of this approach. To prove the real world efficacy of this work it has been applied to a recently drilled carbon capture and sequestration well, estimating the temperature in the target reservoir to be within a 5 °C margin at ~3 km subsurface depth, highlighting the usability and robustness of this methodology in hydrocarbon exploration and future energy transition projects.

8. References

Allen, P., & Allen, J. (2013). Basin analysis: principles and application to petroleum play assessment. In *WileyBlackwell*.

Andrews-Speed, C. P., Oxburgh, E. R., & Cooper, B. A. (1984). Temperatures and Depth-Dependent Heat Flow in Western North Sea. *American Association of Petroleum Geologists Bulletin*, *68*(11), 1764–1781.

Awan, A. R., Teigland, R., & Kleppe, J. (2006). EOR survey in the North Sea. *Proceedings - SPE Symposium on Improved Oil Recovery*, *1*, 294–309. https://doi.org/10.2523/99546-ms

Basso, O., Lascourrèges, J., Jarry, M., & Magot, M. (2005). The effect of cleaning and disinfecting the sampling well on the microbial communities of deep subsurface water samples. *Environmental Microbiology*, *7*(1), 13–21. https://doi.org/10.1111/j.1462-

2920.2004.00660.x

Beardsmore, G., & Cull, J. (2001). Crustal Heat Flow: A Guide to Measurement and Modelling. In *Cambridge University Press*. https://doi.org/10.1017/S0016756803218021

Becker, J. J., Sandwell, D. T., Smith, W. H. F., Braud, J., Binder, B., Depner, J., Fabre, D., Factor, J., Ingalls, S., Kim, S.-H., Ladner, R., Marks, K., Nelson, S., Pharaoh, A., Trimmer, R., Von Rosenberg, J., Wallace, G., & Weatherall, P. (2009). Global Bathymetry and Elevation Data at 30 Arc Seconds Resolution: SRTM30_PLUS. *Marine Geodesy*, *32*(4), 355–371. https://doi.org/10.1080/01490410903297766

Bjørlykke, K., Ramm, M., & Saigal, G. C. (1989). Sandstone diagenesis and porosity modification during basin evolution. *Geologische Rundschau*, *78*(1), 243–268. https://doi.org/10.1007/BF01988363

Blakely, R. J. (1988). Curie temperature isotherm analysis and tectonic implications of aeromagnetic data from Nevada. *Journal of Geophysical Research*, *93*(B10), 11817–11832. https://doi.org/10.1029/JB093iB10p11817

Bonté, D., Van Wees, J. D., & Verweij, J. M. (2012). Subsurface temperature of the onshore Netherlands: New temperature dataset and modelling. *Geologie En Mijnbouw/Netherlands Journal of Geosciences*, *91*(4), 491–515. https://doi.org/10.1017/S0016774600000354

Boulanouar, A., Rahmouni, A., Boukalouch, M., Samaouali, A., Géraud, Y., Harnafi, M., & Sebbani, J. (2013). Determination of Thermal Conductivity and Porosity of Building Stone from Ultrasonic Velocity Measurements. *Geomaterials*, *03*(04), 138–144. https://doi.org/10.4236/gm.2013.34018

Boyer, T. P., Garcia, H. E., Locarnini, R. A., Zweng, M. M., Mishonov, A. V., Reagan, J. R., Antonov, J. I., Baranova, O. K., Biddle, M. M., Johnson, D. R., & Paver, C. R. (2014). 2013 World Ocean Atlas Aids High-Resolution Climate Studies. *Eos, Transactions American Geophysical Union*, *95*(41), 369–370. https://doi.org/10.1002/2014EO410002

Brigaud, F., Chapman, D. S., & Le Douaran, S. (1990). Estimating thermal conductivity in sedimentary basins using lithologic data and geophysical well logs. *American Association of Petroleum Geologists Bulletin*, *74*(9), 1459–1477. https://doi.org/10.1306/0C9B2501-1710-11D7-8645000102C1865D

Brigaud, F., Vasseur, G., & Caillet, G. (1992). Thermal state in the north Viking Graben (North Sea) determined from oil exploration well data. *Geophysics*, *57*(1), 69–88. https://doi.org/10.1190/1.1443190

Cercone, K. R., & Pollack, H. N. (1991). Thermal maturity of the Michigan Basin. *Special Paper of the Geological Society of America*, *256*, 1–12. https://doi.org/10.1130/SPE256-p1

CGG. (2019). *Final Report, CGG18M01:Horda/Tampen PSDM, Offshore Norway - North Viking Graben (NVG)*.

Chadwick, A., Arts, R., Eiken, O., Williamson, P., & Williams, G. (2006). Geophysical Monitoring of the CO2 plume at Sleipnir, North Sea. *Nato Science Series: IV: Earth and Environmental Sciences*, *65*(Advances in the Geological Storage of Carbon Dioxide), 303–314. https://doi.org/10.1007/1-4020-4471-2_25

Christiansson, P., Faleide, J. I., & Berge, A. M. (2000). Crustal structure in the northern North Sea: An integrated geophysical study. *Geological Society Special Publication*, *167*(McKenzie 1978), 15–40. https://doi.org/10.1144/GSL.SP.2000.167.01.02

Christofi, N., & Philip, J. C. (1997). European Microbiology Related to the Subsurface Disposal of Nuclear Waste. In P. S. Amy & D. L. Haldeman (Eds.), *Microbiology of the Terrestrial Deep Subsurface* (pp. 267–268). CRC Press.

Copestake, P., Sims, A., Crittenden, S., Hamar, G., Ineson, J., & Bathurst, P. (2003). The Millennium Atlas : Petroleum Geology of the Central and Northern North Sea. In Dan Evans, C. Graham, A. Armour, & P. Bathurst (Eds.), *Geological Society of London*. Geological Society of London. https://doi.org/https://doi.org/10.1017/S0016756803218124

Cornelius, C. D. (1975). Geothermal aspects of hydrocarbon exploration in the North Sea Area. *Norges Geologiske Undersøkelse Bulletin*, *316*, 29–67.

Cornford, C. (1998). Source Rocks and Hydrocarbons of the North Sea. In K. W. Glennie (Ed.), *Petroleum Geology of the North Sea* (pp. 376–462). Blackwell Science Ltd. https://doi.org/10.1002/9781444313413.ch11

Cox, D. R., Newton, A. M. W., & Huuse, M. (2020). An introduction to seismic reflection data: acquisition, processing and interpretation. In N. Scarselli, J. Adam, & D. Chiarella (Eds.), *Regional geology and tectonics: principles of geologic analysis* (pp. 571–603). Elsevier.

Cozier, M. (2019). CCS takes centre stage. *Greenhouse Gases: Science and Technology*, *9*(6), 1084–1086. https://doi.org/10.1002/ghg.1942

Dahle, H., Garshol, F., Madsen, M., & Birkeland, N.-K. (2008). Microbial community structure analysis of produced water from a high-temperature North Sea oil-field. *Antonie Van Leeuwenhoek*, *93*(1–2), 37–49. https://doi.org/10.1007/s10482-007-9177-z

Davies, J. H. (2013). Global map of solid Earth surface heat flow. *Geochemistry, Geophysics, Geosystems*, *14*(10), 4608–4622. https://doi.org/10.1002/ggge.20271

Davison, I., & Underhill, J. R. (2012). Tectonics and Sedimentation in Extensional Rifts. In D. Gao (Ed.), *Tectonics and Sedimentation* (pp. 15–42). American Association of Petroleum Geologists. https://doi.org/10.1306/13351547M1001556

Duffaut, K., Hokstad, K., Kyrkjeb, R., & Wiik, T. (2018). A simple relationship between thermal conductivity and seismic interval velocity. *Leading Edge*, *37*(5), 381–385. https://doi.org/10.1190/tle37050381.1

Eberhart-Phillips, D., Han, D. H., & Zoback, M. D. (1989). Empirical relatlonshlps among seismic velocity, effective pressure, porosity, and clay content in sandstone. *Geophysics*, *54*(1), 82–89. https://doi.org/doi.org/10.1190/1.1442580

Eiken, O., Ringrose, P., Hermanrud, C., Nazarian, B., Torp, T. A., & Høier, L. (2011). Lessons Learned from 14 years of CCS Operations: Sleipner, In Salah and Snøhvit. *Energy Procedia*, *4*, 5541–5548. https://doi.org/10.1016/j.egypro.2011.02.541

Esteban, L., Pimienta, L., Sarout, J., Piane, C. D., Haffen, S., Geraud, Y., & Timms, N. E. (2015). Study cases of thermal conductivity prediction from P-wave velocity and porosity.

Geothermics, *53*, 255–269. https://doi.org/10.1016/j.geothermics.2014.06.003

Evans, T. R. (1977). Thermal Properties of North Sea Rocks. *Log Analyst*, *18*(2), 3–12.

Evans, T. R., & Coleman, N. C. (1974). North Sea geothermal gradients. *Nature*, *247*(5435), 28–30. https://doi.org/10.1038/247028a0

Fichler, C., Odinsen, T., Rueslåtten, H., Olesen, O., Vindstad, J. E., & Wienecke, S. (2011). Crustal inhomogeneities in the Northern North Sea from potential field modeling: Inherited structure and serpentinites? *Tectonophysics*, *510*(1–2), 172–185. https://doi.org/10.1016/j.tecto.2011.06.026

Fossen, H., Pedersen, R. B., Bergh, S., & Andresen, A. (2008). Creation of a mountain chain. In I. B. Ramberg, I. Bryhni, A. Nøttvedt, & K. Rangnes (Eds.), *The Making of a Land: geology of Norway* (pp. 178–232). The Norwegian Geological Association.

Fuchs, S., & Balling, N. (2016). Improving the temperature predictions of subsurface thermal models by using high-quality input data. Part 2: A case study from the Danish-German border region. *Geothermics*, *64*, 1–14. https://doi.org/10.1016/j.geothermics.2016.04.004

Fuchs, S., & Förster, A. (2013). Well-log based prediction of thermal conductivity of sedimentary successions: A case study from the north german basin. *Geophysical Journal International*, *196*(1), 291–311. https://doi.org/10.1093/gji/ggt382

Galson, D. A., Wilson, N. P., Schärli, U., & Rybach, L. (1987). A comparison of the divided-bar and QTM methods of measuring thermal conductivity. *Geothermics*, *16*(3), 215–226. https://doi.org/10.1016/0375-6505(87)90001-0

Gautier, D. L. (2005). *Kimmeridgian shales total petroleum system of the North Sea graben province*. US Geological Survey.

Gegenhuber, N., & Schoen, J. (2012). New approaches for the relationship between compressional wave velocity and thermal conductivity. *Journal of Applied Geophysics*, *76*, 50–55. https://doi.org/10.1016/j.jappgeo.2011.10.005

Goff, J. C. (1983). Hydrocarbon generation and migration from Jurassic source rocks in the E Shetland Basin and Viking Graben of the northern North Sea. *Journal - Geological Society London*, *140*(3), 445–474. https://doi.org/10.1144/gsjgs.140.3.0445

Gosnold, W., & Panda, B. (2002). *The Global Heat Flow Database of the International Heat Flow Commission*. https://doi.org/http://doi.org/10.17616/R3G305

Grad, M., & Tiira, T. (2009). The Moho depth map of the European Plate. *Geophysical Journal International*, *176*(1), 279–292. https://doi.org/10.1111/j.1365-246X.2008.03919.x

Gu, Y., Rühaak, W., Bär, K., & Sass, I. (2017). Using seismic data to estimate the spatial distribution of rock thermal conductivity at reservoir scale. *Geothermics*, *66*, 61–72. https://doi.org/10.1016/j.geothermics.2016.11.007

Haaland, H. J., Furnes, H., & Martinsen, O. J. (2000). Paleogene tuffaceous intervals, Grane Field (Block 25/11), Norwegian North Sea: their depositional, petrographical, geochemical character and regional implications. *Marine and Petroleum Geology*, *17*(1), 101–118. https://doi.org/10.1016/S0264-8172(99)00009-4

Harper, M. L. (1971). Approximate geothermal gradients in the North Sea basin. *Nature*, *230*(5291), 235–236. https://doi.org/10.1038/230235a0

Hartmann, A. Ã., Rath, V., & Clauser, C. (2005). Thermal conductivity from core and well log data. *International Journal of Rock Mechanics and Mining Sciences*, *42*(7-8 SPEC. ISS.), 1042–1055. https://doi.org/10.1016/j.ijrmms.2005.05.015

Hasterok, D. (2010). *Thermal State of Continental and Oceanic Lithosphere*. The University of Utah.

Hasterok, D., Chapman, D. S., & Davis, E. E. (2011). Oceanic heat flow: Implications for global heat loss. *Earth and Planetary Science Letters*, *311*(3–4), 386–395. https://doi.org/10.1016/j.epsl.2011.09.044

Hazen, T. C. (1997). Bioremediation. In P. S. Amy & D. L. Haldeman (Eds.), *The Microbiology of the Terrestrial Deep Subsurface* (pp. 247–266). CRC Press.

Hokstad, K., Tašárová, Z. A., Clark, S. A., Kyrkjebø, R., Duffaut, K., Fichler, C., & Wiik, T. (2017). Radiogenic heat production in the crust from inversion of gravity and magnetic data. *Norsk Geologisk Tidsskrift*, *97*(3), 241–254. https://doi.org/10.17850/njg97-3-04

Horai, K. (1982). Thermal Conductivity of Sediments and Igneous Rocks Recovered during Deep Sea Drilling Project Leg 60. In D. M. Hussong & S. Uyeda (Eds.), *Initial Reports of the Deep Sea Drilling Project, 60* (Vol. 60, pp. 807–834). U.S. Government Printing Office. https://doi.org/10.2973/dsdp.proc.60.149.1982

Houbolt, J. J. H. C., & Wells, P. R. A. (1980). Estimation of Heat Flow in Oil Wells Based on Relation Between Heat Conductivity and Sound Velocity. *AAPG Bulletin*, *65*(7), 1360–1361.

Jones, I. F. (2018). *Velocities, Imaging, and Waveform Inversion – The evolution of characterizing the Earth's subsurface*. EAGE Publications.

Jorand, R., Clauser, C., Marquart, G., & Pechnig, R. (2015). Statistically reliable petrophysical properties of potential reservoir rocks for geothermal energy use and their relation to lithostratigraphy and rock composition: The NE Rhenish Massif and the Lower Rhine Embayment (Germany). *Geothermics*, *53*, 413–428. https://doi.org/10.1016/j.geothermics.2014.08.008

Justwan, H., Meisingset, I., Dahl, B., & Isaksen, G. H. (2006). Geothermal history and petroleum generation in the Norwegian South Viking Graben revealed by pseudo-3D basin modelling. *Marine and Petroleum Geology*, *23*(8), 791–819. https://doi.org/10.1016/j.marpetgeo.2006.07.001

Kubala, M., Bastow, M., Thompson, S., Scotchman, I., & Oygard, K. (2003). Geothermal regime, petroleum generation and migration. In D Evans, C. Graham, A. Armour, & P. Bathurst (Eds.), *The Millenium Atlas: Petroleum Geology of the Central and Northern North Sea* (pp. 285–315). The Geological Society of London.

Landrø, M., Solheim, O. A., Hilde, E., Ekren, B. O., & Strønen, L. K. (1999). The Gullfaks 4D seismic study. *Petroleum Geoscience*, *5*(3), 213–226.

https://doi.org/10.1144/petgeo.5.3.213

Leadholm, R. H., Ho, T. T. Y., & Sahai, S. K. (1985). Heat flow, geothermal gradients and maturation modelling on the Norwegian continental shelf using computer methods. In *Petroleum Geochemistry in Exploration of the Norwegian Shelf* (pp. 131–143). Springer Netherlands. https://doi.org/10.1007/978-94-009-4199-1_9

Lee, M. W. (2003). Elastic properties of overpressured and unconsolidated sediments. In *U.S. Geological Survey Bulletin* (Vol. 2214). https://pubs.er.usgs.gov/publication/b2214

Licciardi, A., England, R. W., Piana Agostinetti, N., & Gallagher, K. (2020). Moho depth of the British Isles: a probabilistic perspective. *Geophysical Journal International*, *221*(2), 1384–1401. https://doi.org/10.1093/gji/ggaa021

Lister, C. R. B. (1972). On the Thermal Balance of a Mid-Ocean Ridge. *Geophysical Journal International*, *26*(5), 515–535. https://doi.org/10.1111/j.1365-246X.1972.tb05766.x

Locarnini, R. A., Mishonov, A. V, Antonov, J. I., Boyer, T. P., Garcia, H. E., Baranova, O. K., Zweng, M. M., Paver, C. R., Reagan, J. R., Johnson, D. R., Hamilton, M., & Seidov, D. (2013). *WORLD OCEAN ATLAS 2013: Temperature Volume 1* (Vol. 1, Issue NOAA Atlas NESDID 81). https://doi.org/10.7289/V55X26VD

Løseth, H., Øygarden, B., Nygård, A., & Raulline, B. (2016). Reply to Discussion on 'Late Cenozoic geological evolution of the northern North Sea: development of a Miocene unconformity reshaped by large-scale Pleistocene sand intrusion', Journal of the Geological Society , 170, 133–145 [Article]. *Journal of the Geological Society*, *173*(2), 394–397. https://doi.org/10.1144/jgs2015-104

Løseth, H., Raulline, B., & Nygård, A. (2013). Late Cenozoic geological evolution of the northern North Sea: development of a Miocene unconformity reshaped by large-scale Pleistocene sand intrusion. *Journal of the Geological Society*, *170*(1), 133–145. https://doi.org/10.1144/jgs2011-165

Lucazeau, F. (2019). Analysis and Mapping of an Updated Terrestrial Heat Flow Data Set. *Geochemistry, Geophysics, Geosystems*, *20*(8), 4001–4024. https://doi.org/10.1029/2019GC008389

Lucazeau, F., & Le Douaran, S. (1985). The blanketing effect of sediments in basins formed by extension: a numerical model. Application to the Gulf of Lion and Viking graben. *Earth and Planetary Science Letters*, *74*(1), 92–102. https://doi.org/10.1016/0012-821X(85)90169-4

Lucazeau, Francis, Brigaud, F., & Bouroullec, J. L. (2004). High-resolution heat flow density in the lower Congo basin. *Geochemistry, Geophysics, Geosystems*, *5*(3), Q03001. https://doi.org/10.1029/2003GC000644

Mareschal, J., & Jaupart, C. (2013). Radiogenic heat production, thermal regime and evolution of continental crust. *Tectonophysics*, *609*, 524–534. https://doi.org/10.1016/j.tecto.2012.12.001

Mavko, G., Mukerji, T., & Dvorkin, J. (2009). *The rock physics handbook : tools for seismic analysis of porous media* (T. Mukerji 1965-, J. Dvorkin 1953-, T. Mukerji 1965- author, & J. Dvorkin 1953- author (Eds.); 2nd ed.). Cambridge : Cambridge University Press.

Meert, J. G., & Torsvik, T. H. (2003). The making and unmaking of a supercontinent: Rodinia revisited. *Tectonophysics*, *375*(1–4), 261–288. https://doi.org/10.1016/S0040-1951(03)00342-1

Mielke, P., Bär, K., & Sass, I. (2017). Determining the relationship of thermal conductivity and compressional wave velocity of common rock types as a basis for reservoir characterization. *Journal of Applied Geophysics*, *140*, 135–144. https://doi.org/10.1016/j.jappgeo.2017.04.002

Nadeau, P. H. (2011). Earth's energy "Golden Zone": a synthesis from mineralogical research. *Clay Minerals*, *46*(1), 1–24. https://doi.org/10.1180/claymin.2011.046.1.1

Nottvedt, A., Gabrielsen, R. H., & Steel, R. J. (1995). Tectonostratigraphy and sedimentary architecture of rift basins, with reference to the northern North Sea. *Marine and Petroleum Geology*, *12*(8), 881–901. https://doi.org/10.1016/0264-8172(95)98853-W

Philip, G. M., & Watson, D. F. (1982). A Precise Method for Determining Contoured Surfaces. *The APPEA Journal*, *22*(1), 205–212. https://doi.org/doi.org/10.1071/AJ81016

Pimienta, L., Klitzsch, N., & Clauser, C. (2018). Comparison of thermal and elastic properties of sandstones: Experiments and theoretical insights. *Geothermics*, *76*(June), 60–73. https://doi.org/10.1016/j.geothermics.2018.06.005

Pollack, H. N., Hurter, S. J., & Johnson, J. R. (1993). Heat flow from the Earth's interior: Analysis of the global data set. *Reviews of Geophysics*, *31*(3), 267. https://doi.org/10.1029/93RG01249

Popov, Y. A., Pribnow, D. F. C., Sass, J. H., Williams, C. F., & Burkhardt, H. (1999). Characterization of rock thermal conductivity by high-resolution optical scanning. *Geothermics*, *28*(2), 253–276. https://doi.org/10.1016/S0375-6505(99)00007-3

Popov, Y., Tertychnyi, V., Romushkevich, R., Korobkov, D., & Pohl, J. (2003). Interrelations Between Thermal Conductivity and Other Physical Properties of Rocks: Experimental Data. *Pure and Applied Geophysics*, *160*(5), 1137–1161. https://doi.org/10.1007/PL00012565

Posamentier, H. W. (2004). Seismic Geomorphology: Imaging Elements of Depositional Systems from Shelf to Deep Basin Using 3D Seismic Data: Implications for Exploration and Development. *Geological Society, London, Memoirs*, *29*(1), 11–24. https://doi.org/10.1144/GSL.MEM.2004.029.01.02

Prada, M., Lavoué, F., Saqab, M. M., O'Reilly, B. M., Lebedev, S., Walsh, J. J., & Childs, C. (2019). Across-axis variations in petrophysical properties of the North Porcupine Basin, offshore Ireland: New insights from long-streamer traveltime tomography. *Basin Research*, *31*(1), 59–76. https://doi.org/10.1111/bre.12308

Pribnow, D. F. C., Kinoshita, M., & Stein, C. . (2000). Thermal data collection and heat flow recalculations for ODP Legs 101-180. In *Institute for Joint Geoscientific Research*. http://www-odp.tamu.edu/publications/heatflow/

Purvis, S., Caughtry, N., Mann, J., & Rumyantseva, A. (2018). *Northern Viking Graben Well Study* (Issue 10592).

Rajaram, M., Anand, S. P., Hemant, K., & Purucker, M. E. (2009). Curie isotherm map of Indian subcontinent from satellite and aeromagnetic data. *Earth and Planetary Science Letters*, *281*(3–4), 147–158. https://doi.org/10.1016/j.epsl.2009.02.013

Ritter, U., Zielinski, G. W., Weiss, H. M., Zielinski, R. L. B., & Sættem, J. (2004). Heat flow in the Vøring Basin, Mid-Norwegian Shelf. *Petroleum Geoscience*, *10*(4), 353–365. https://doi.org/10.1144/1354-079303-616

Rüpke, L. H., Schmalholz, S. M., Schmid, D. W., & Podladchikov, Y. Y. (2008). Automated thermotectonostratigraphic basin reconstruction: Viking Graben case study. *AAPG Bulletin*, *92*(3), 309–326. https://doi.org/10.1306/11140707009

Sarkar, A. D. (2020). *Reflection Seismic Thermometry*. University of Manchester.

Sarkar, A. D., & Huuse, M. (2018). Subsurface Temperature Prediction From Seismic Measurements: A 3-D Seismic Case Study From The Lüderitz Basin, Offshore Namibia. *AAPG International Conference and Exhibition*. https://www.searchanddiscovery.com/abstracts/html/2018/ice2018/abstracts/2965337.html

Schön, J. H. (2015a). Appendix. In *Physical Properties of Rocks* (Vol. 65, Issue 1995, pp. 445–453). https://doi.org/10.1016/B978-0-08-100404-3.10000-9

Schön, J. H. (2015b). Thermal Properties. In *Developments in Petroleum Science* (Vol. 65, pp. 369–414). https://doi.org/10.1016/B978-0-08-100404-3.00009-3

The GEBCO_2019 Grid - a continuous terrain model of the global oceans and land. (2019). In *GEBCO Bathymetric Compilation Group*. British Oceanographic Data Centre, National Oceanography Centre, NERC, UK. https://doi.org/10.5285/836f016a-33be-6ddc-e053-6c86abc0788e

Velde, B. (1996). Compaction trends of clay-rich deep sea sediments. *Marine Geology*, *133*(3–4), 193–201. https://doi.org/10.1016/0025-3227(96)00020-5

Wangen, M. (1995). The blanketing effect in sedimentary basins. *Basin Research*, *7*(4), 283–298. https://doi.org/10.1111/j.1365-2117.1995.tb00118.x

Warner, M., Ratcliffe, A., Nangoo, T., Morgan, J., Umpleby, A., Shah, N., Vinje, V., Štekl, I., Guasch, L., Win, C., Conroy, G., & Bertrand, A. (2013). Anisotropic 3D full-waveform inversion. *Geophysics*, *78*(2), R59–R80. https://doi.org/10.1190/geo2012-0338.1

Watson, D. F., & Philip, G. M. (1985). A refinement of inverse distance weighted interpolation. *Geoprocessing*, *2*(4), 315–327.

Zamora, M., Vo-Thanh, D., Bienfait, G., & Poirier, J. P. (1993). An empirical relationship between thermal conductivity and elastic wave velocities in sandstone. *Geophysical Research Letters*, *20*(16), 1679–1682. https://doi.org/10.1029/92GL02460

Ziegler, P. A. (1992). North Sea rift system. *Tectonophysics*, *208*(1–3), 55–75. https://doi.org/10.1016/0040-1951(92)90336-5

9. Figures

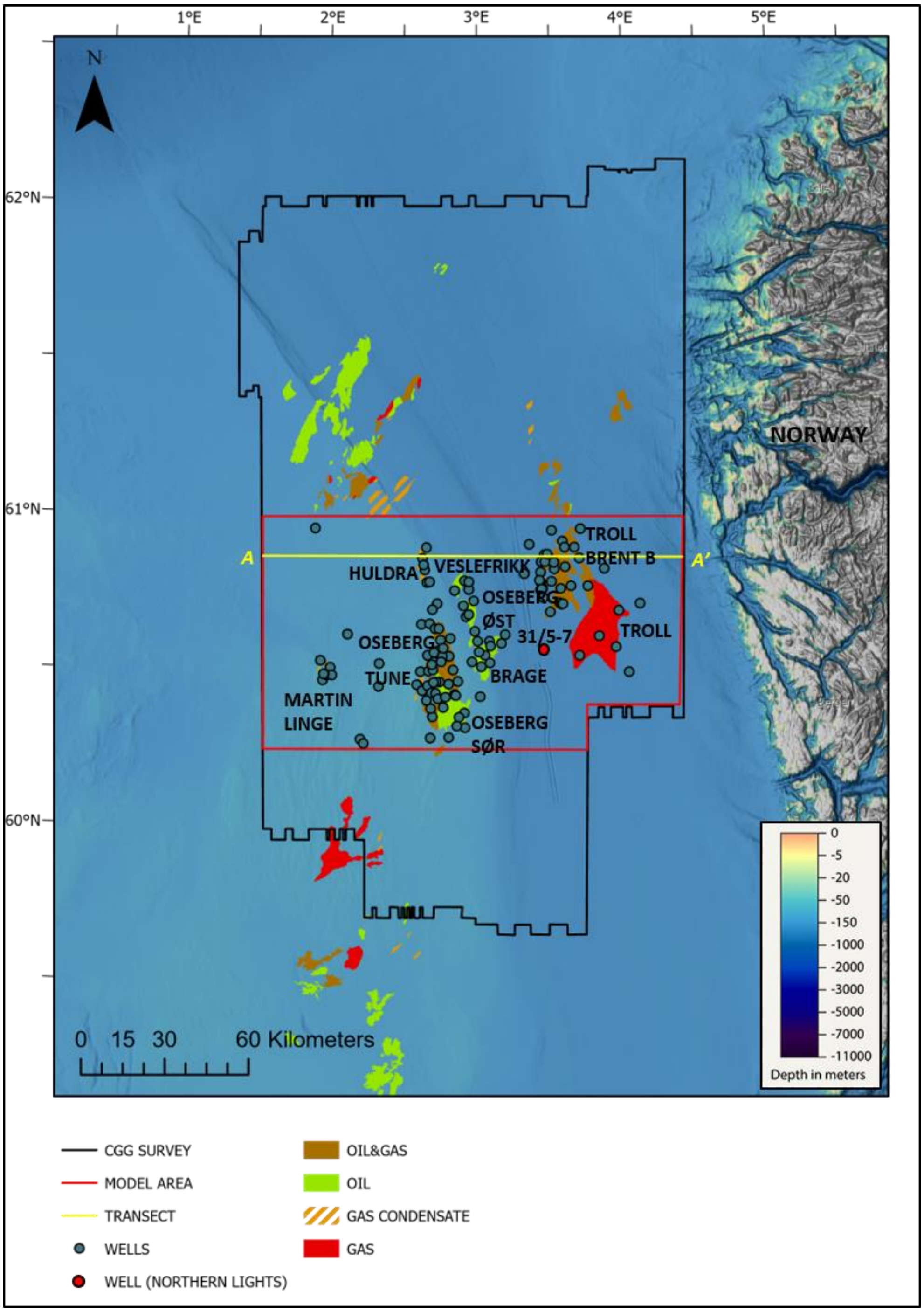

Figure 1: Study area in the northern North Sea outlining the extent of the CGG North Viking Graben survey offshore the Norwegian continental shelf. Some key fields in the study area are named for reference. Thermal model area displayed in red. Transect A-A' based on North Viking Graben type section (Copestake et al., 2003)*. Exploration wells displayed are used for calibration. Northern Lights CCS test well 31/5-7 also displayed (red circle) (between Brage and Troll fields). Bathymetry from GEBCO ("The GEBCO_2019 Grid - a continuous terrain model of the global oceans and land.," 2019).*

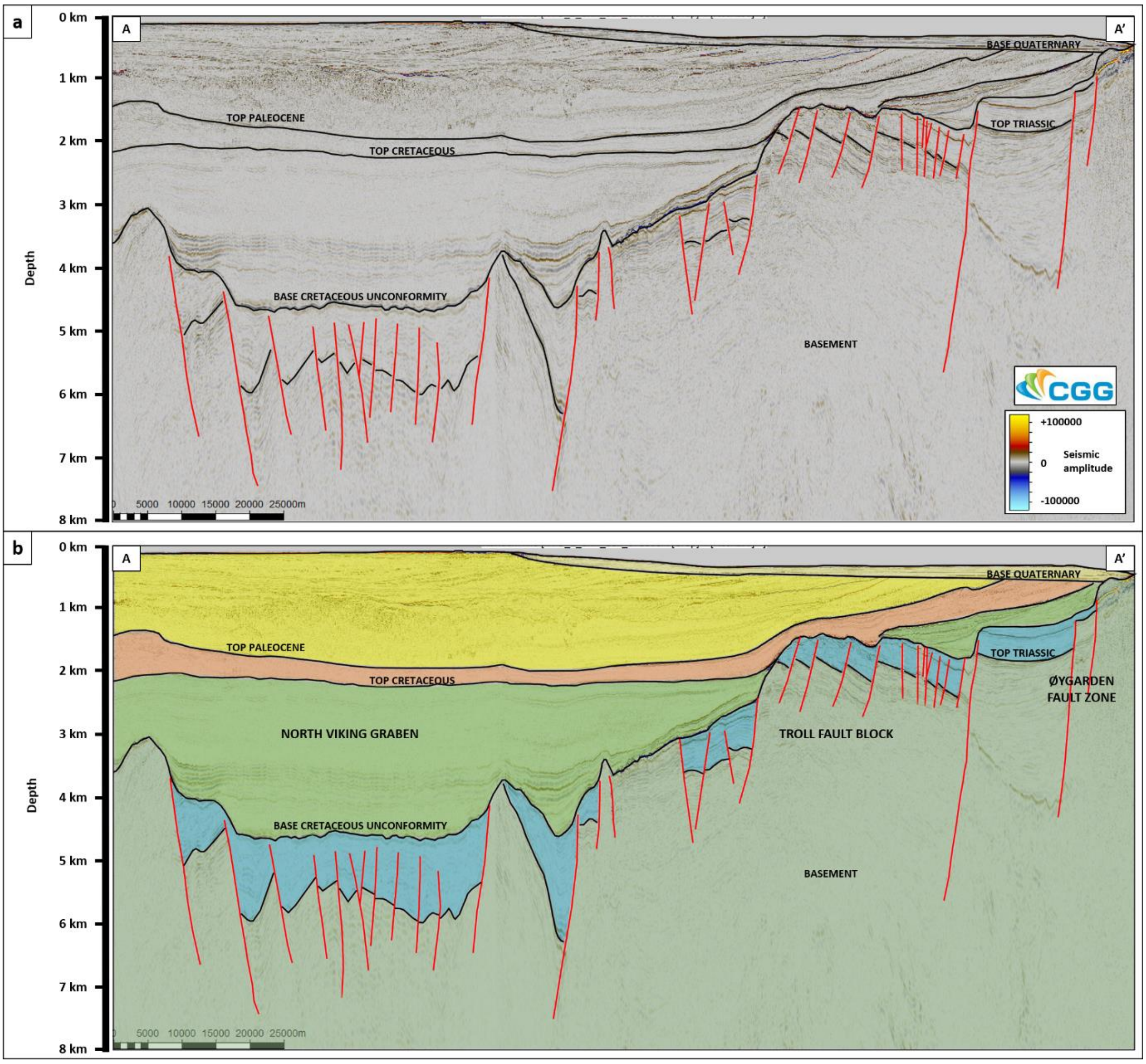

Figure 2: (a) East West transect (A-A' in Fig. 1) displaying reflection seismic data, annotated with major chronostratigraphic surfaces and structures of note. (b) Overlay of major intervals highlighting the geometry of the North Viking Graben in the west of the model area, with tilted fault blocks apparent. The study area is bounded to the west by the East Shetland Basin, with the eastern limits coinciding with the Horda platform. Adapted from (Copestake et al., 2003).

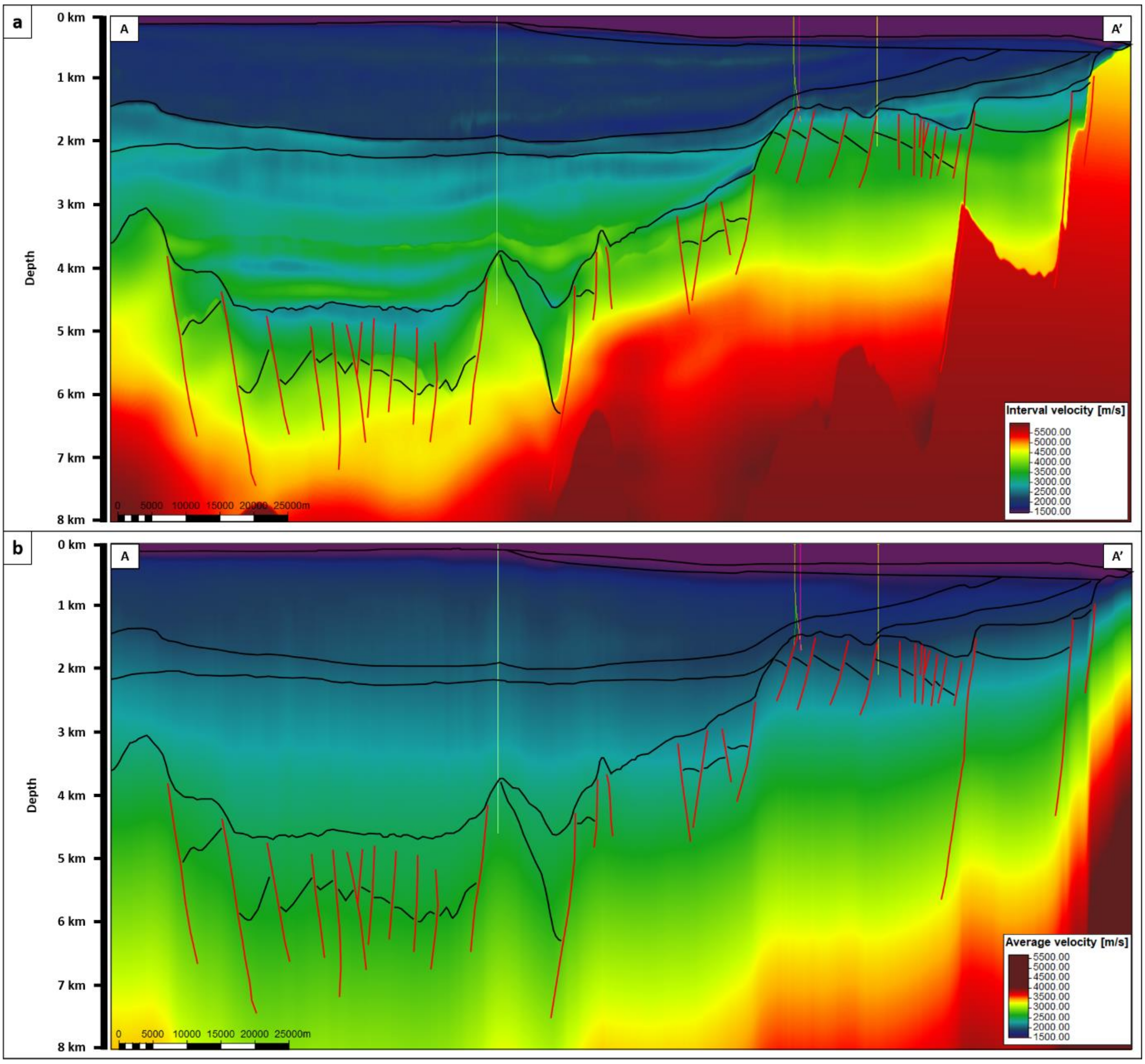

Figure 3: (a) Transect displaying interval velocities from FWI velocity model, overlain with structures. With adherence to well data (well paths shown in various colours), this velocity model can be seen to show detail, corresponding with major structural and stratigraphic interfaces. Basement is marked by the transition to velocities ≥6000 m s^{-1} (Christiansson et al., 2000; Fichler et al., 2011). (b) Transect displaying average velocities from FWI velocity model used to condition thermal model, also shown with well paths.

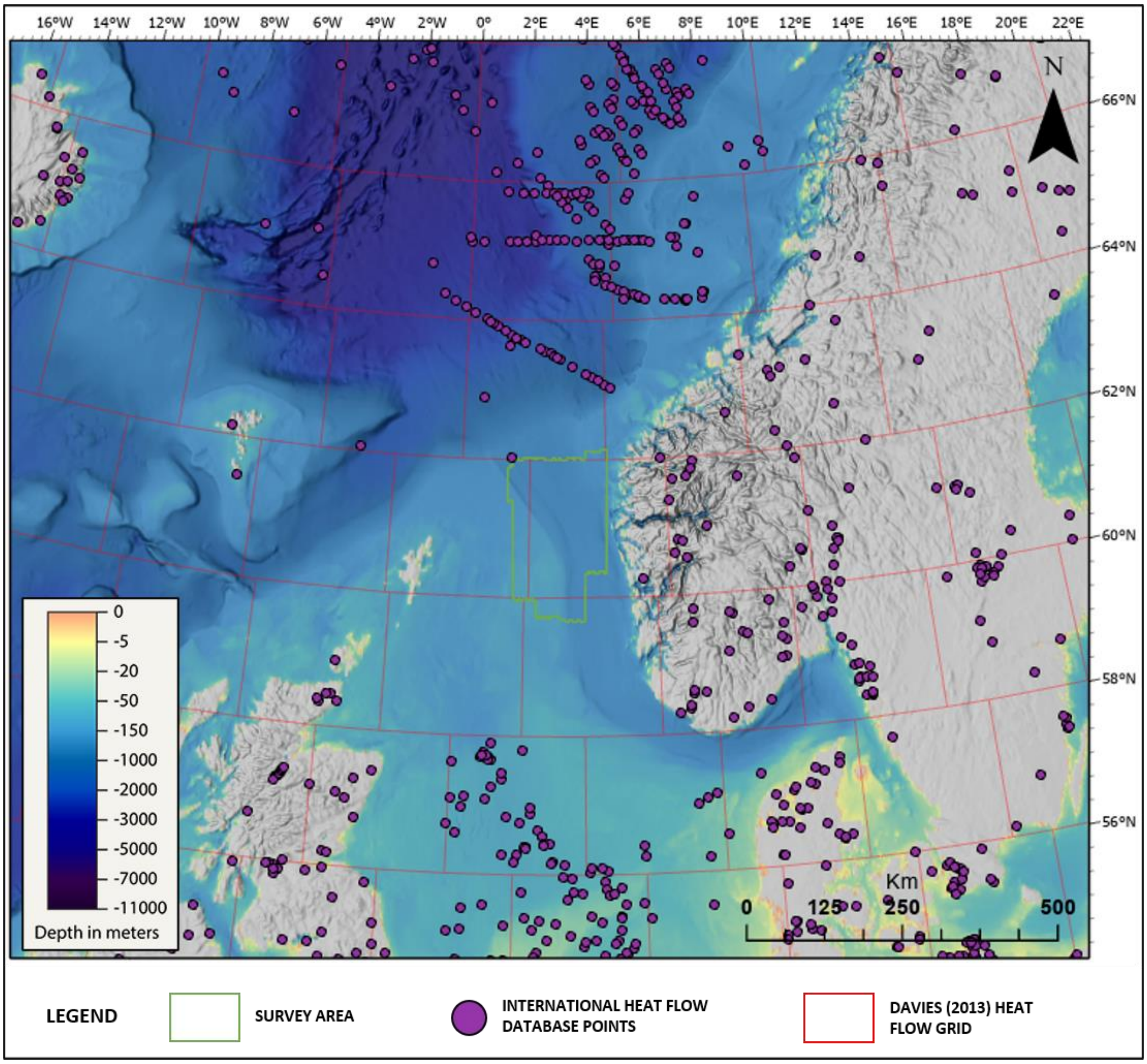

Figure 4: Existing heat flow data from the International Heat Flow Database shows a scarcity of data in the model area (Gosnold & Panda, 2002). Relying on published heat flow grids such as the Davies (2013) shown above demonstrates the coarseness of the data when compared to the scale of the model area (Davies, 2013).

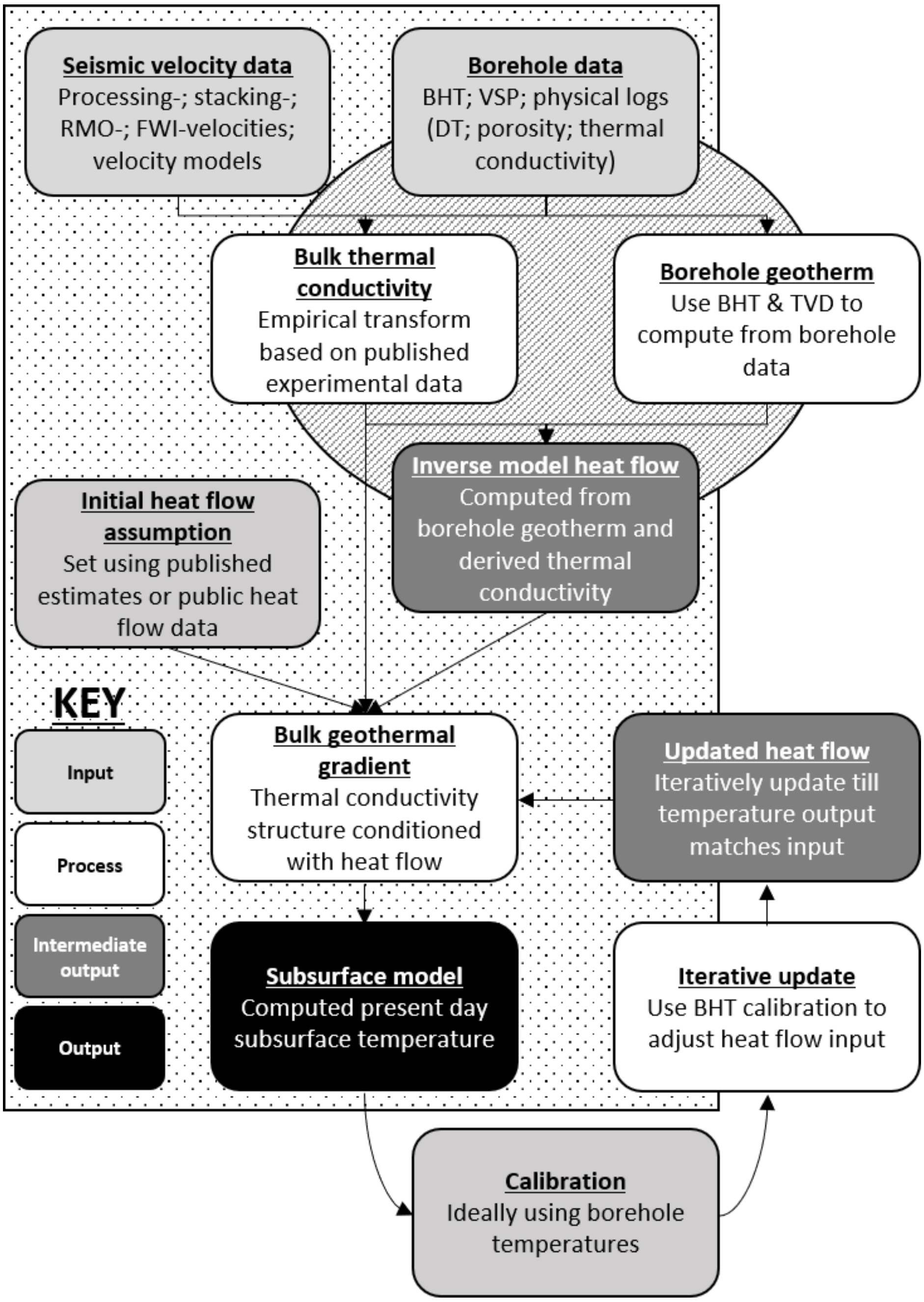

Figure 5: Model building workflow displayed in terms of input, processing steps and outputs/deliverables. There are two main pathways, a forward modelling pathway (demarcated with the dotted background polygon) where seismic data is used to simulate BHTs; and an inverse modelling pathway (demarcated with the hashed background polygon) where BHTs are used to determine the heat flow conditions needed for it. This allows for an iterative final forward modelling pathway utilising the derived heat flow to arrive at a subsurface temperature model representative of present-day conditions.

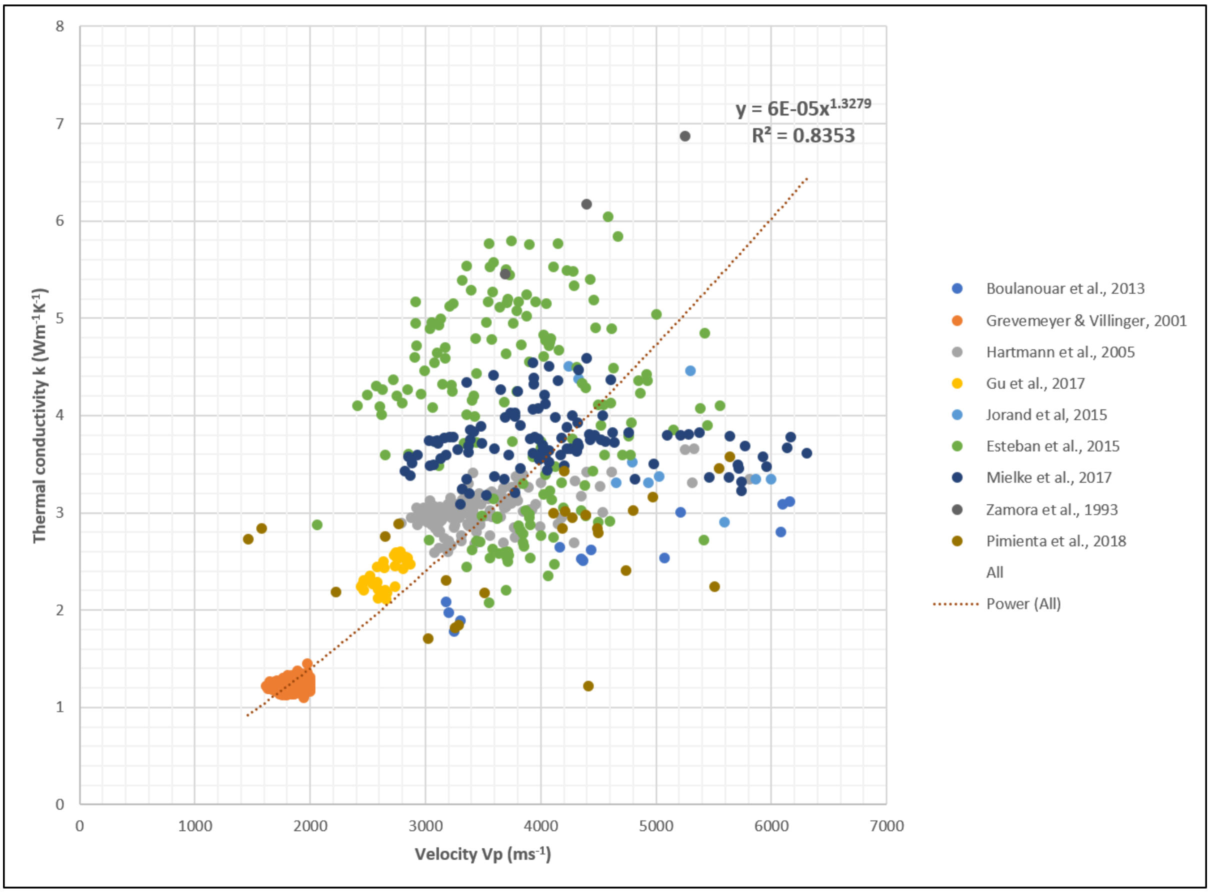

Figure 6: Bulk shift transform from velocity to thermal conductivity derived from experimental data published in the literature. All points displayed are wet samples with laboratory measurements of both velocity and thermal conductivity having been done with similar tools. This is to both reflect the presence of fluids in the subsurface and to also reduce the variables between displayed data respectively.

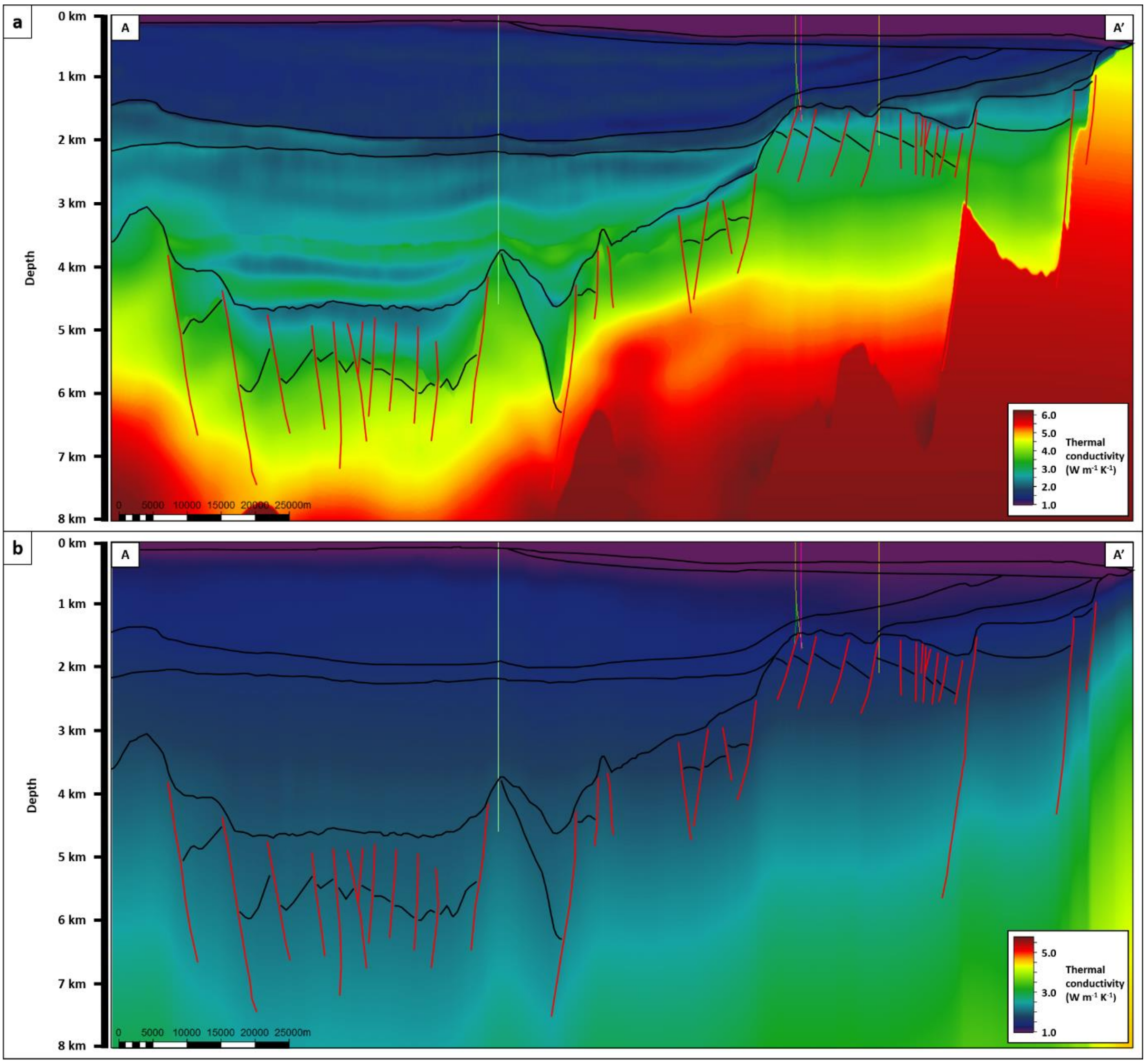

Figure 7: (a) Thermal conductivity from interval velocities with wells displayed. (b) Thermal conductivity from average velocities.

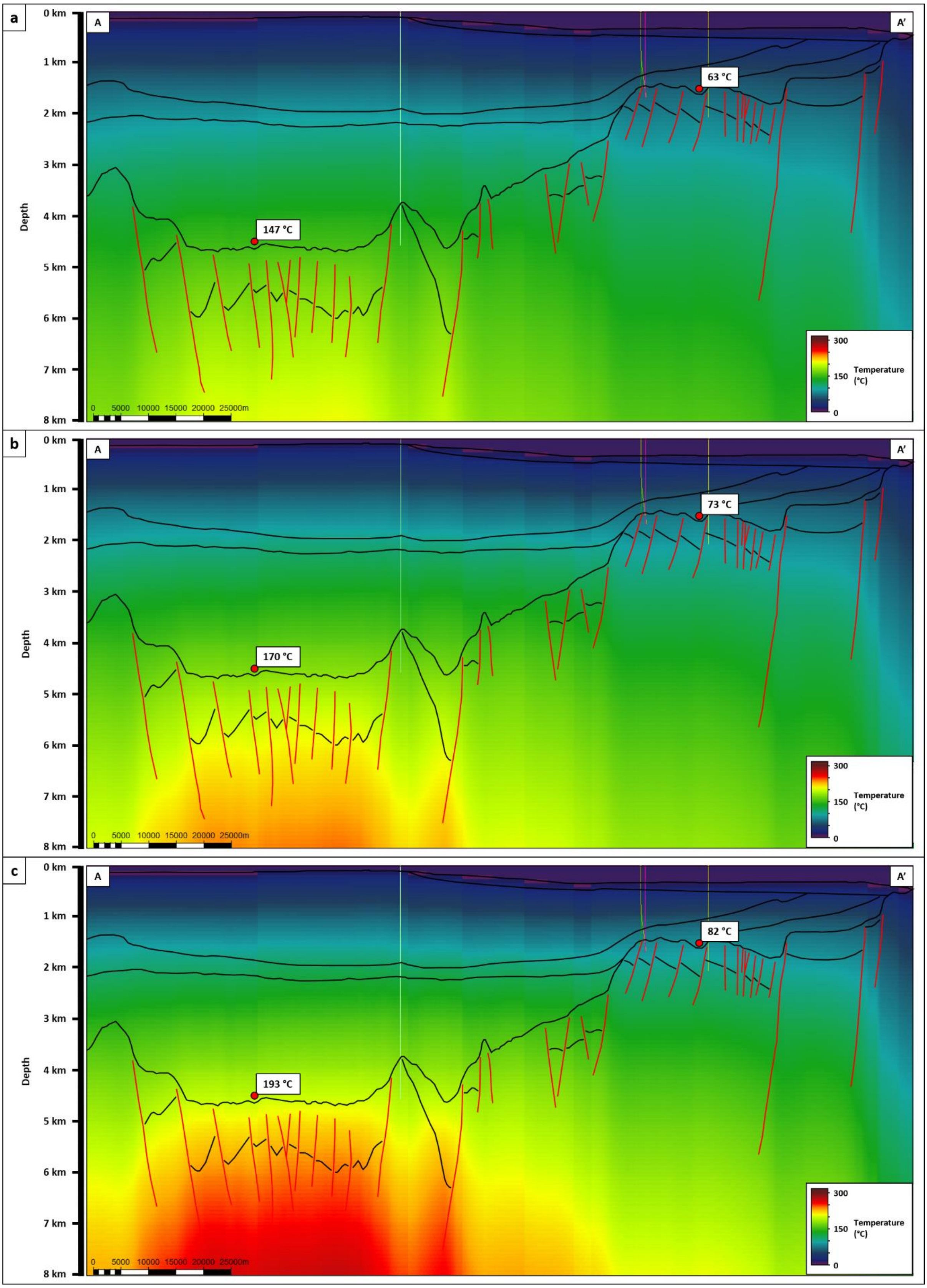

Figure 8: Forward modelling temperature prediction profiles with transect A-A′ overlain for (a) low case (60 mW m^{-2}); (b) mid case (70 mW m^{-2}); & (c) high case (80 mW m^{-2}) heat flow scenarios respectively. Temperature readings in the graben centre and on the graben flank are shown for reference. Highest temperatures are observed in the heart of the graben.

Block like appearance is an artefact of the dimensions of the individual voxels comprising the thermal model pillar grid used to represent the subsurface.

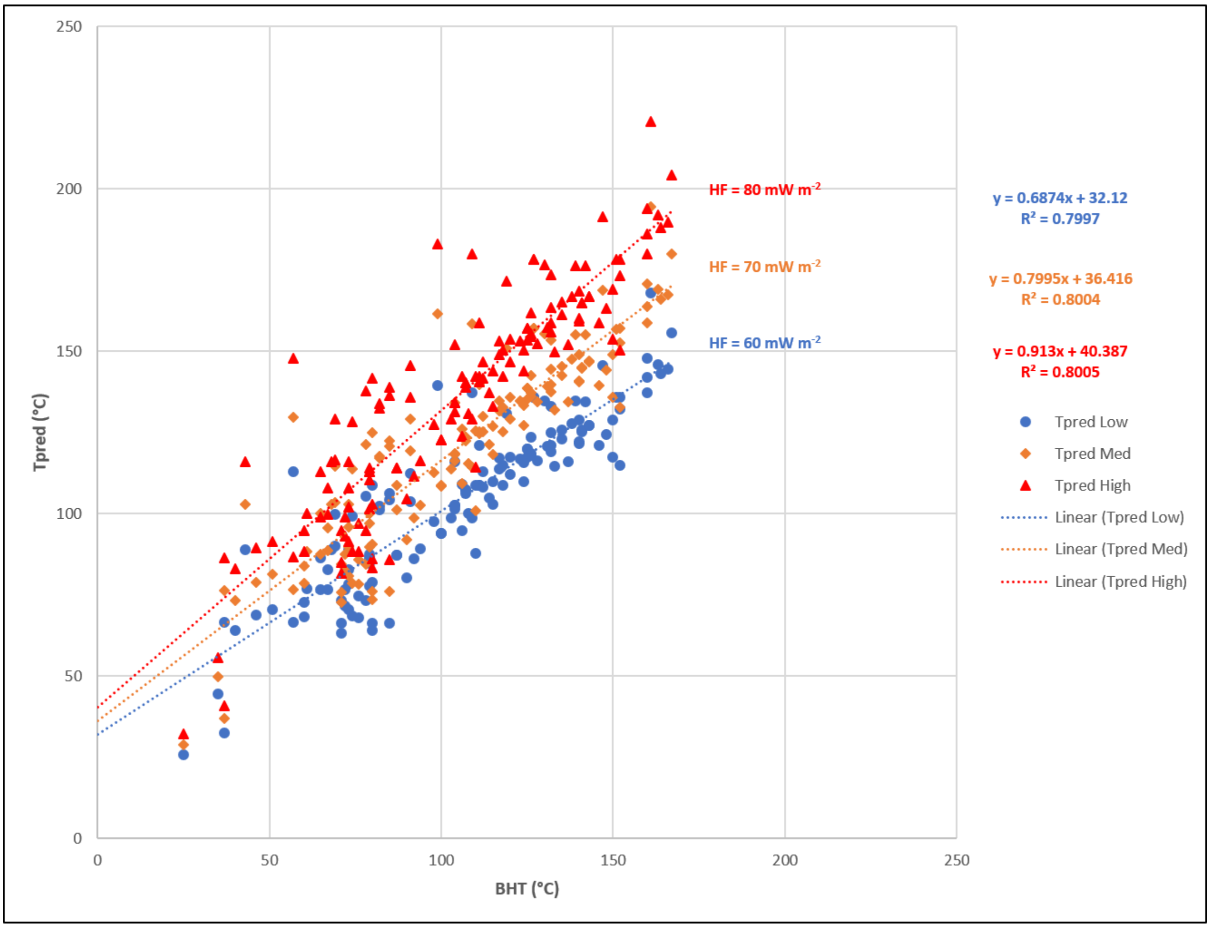

Figure 9: Cross plot of BHT against predicted temperatures (Tpred) for each of the three forward modelling starting conditions for heat flow (low; mid and high case corresponding to 60; 70 and 80 mW m^{-2} respectively). With increasing input heat flow a corresponding increase is seen in the gradient of the regression line through that set of points.

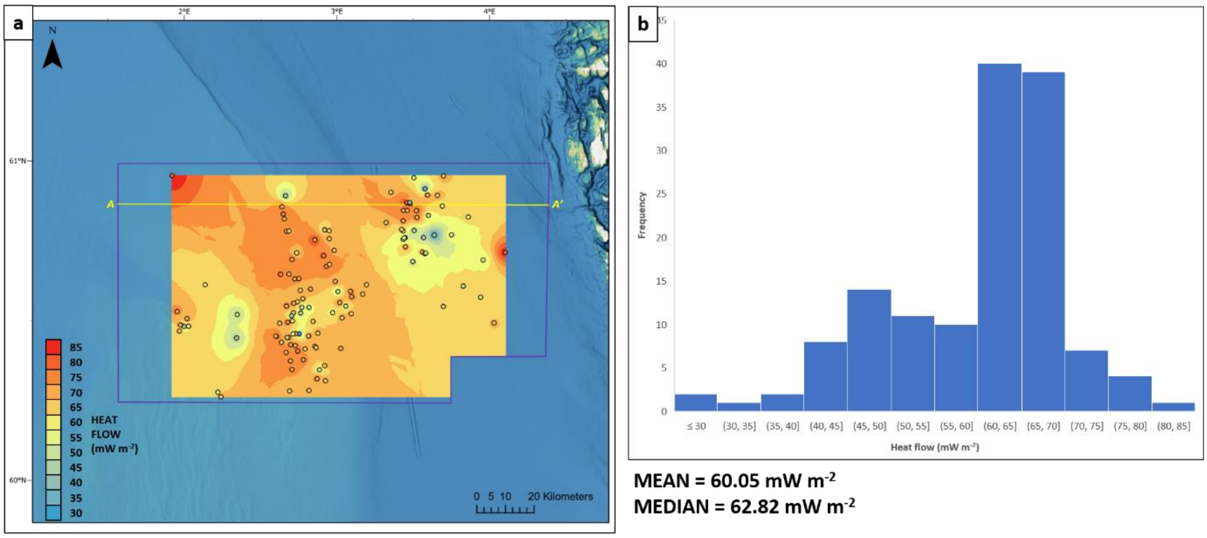

Figure 10: Inverse modelling of heat flow at each well location from BHT and TVD. (a) This data is used to krige heat flow across the model area. Kriged heat flow shows lateral variability at much higher resolution than published global grids. (b) Histogram of heat flow modelled for each well with summary statistics.

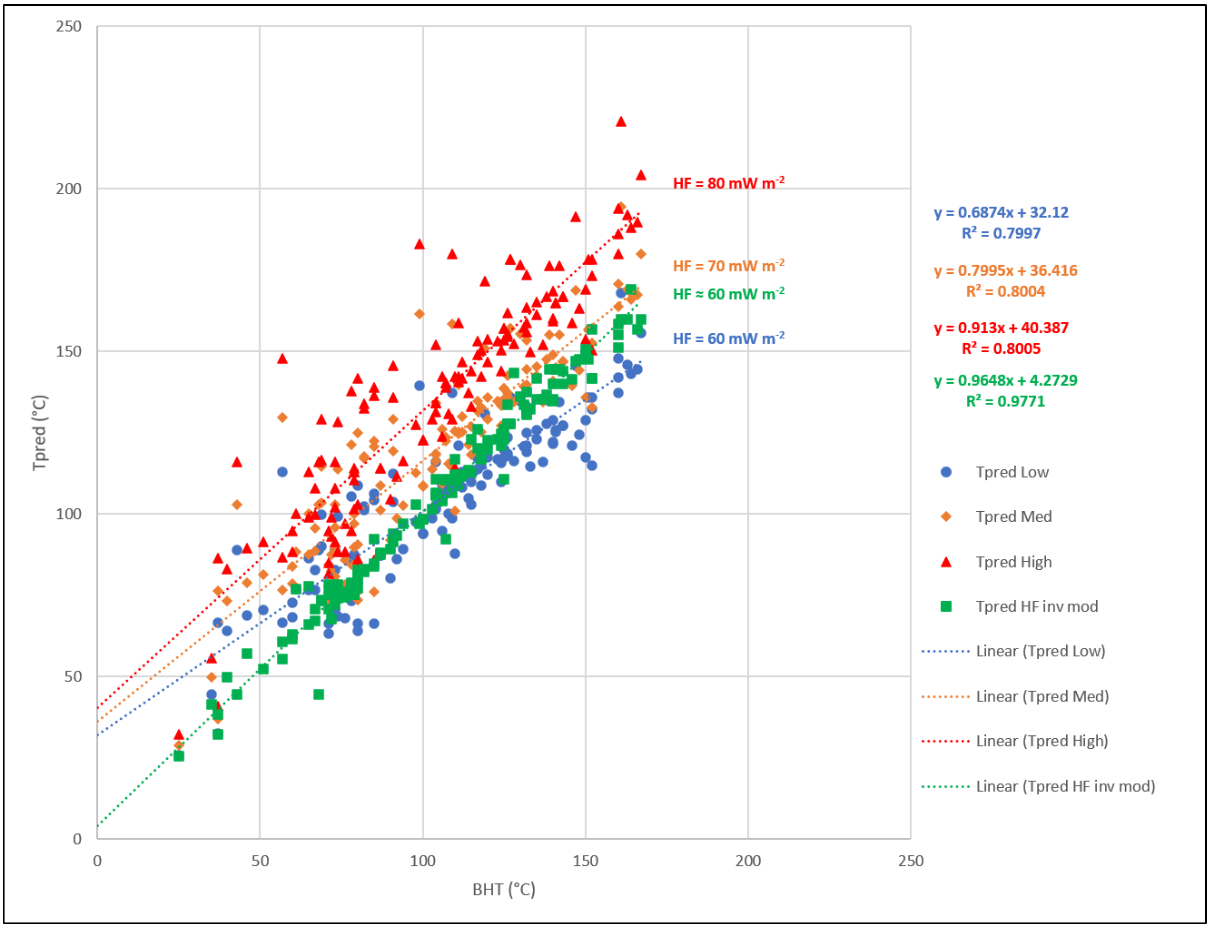

Figure 11: Cross plot of BHT against predicted temperatures (Tpred) with model results using inverse modelling of heat flow across the area displayed (green squares). It becomes apparent from the chi-squared for this regression that not only is there a good statistical fit,

the results have a gradient verging on 1:1 as would be expected for results best reflecting the actual subsurface temperature conditions. Furthermore, the spread of points is much narrower for this modelling outcome.

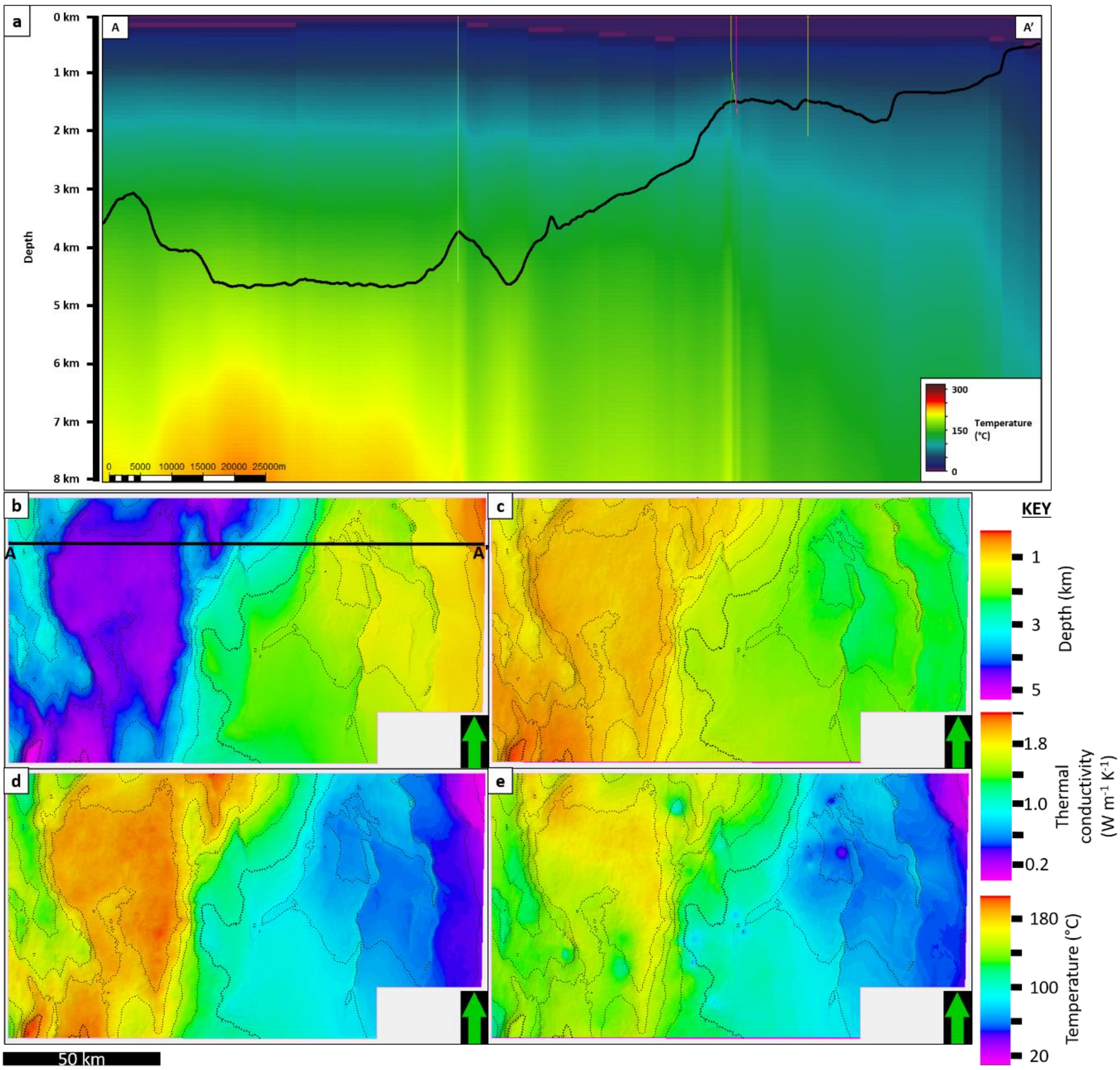

Figure 12: (a) Final temperature model produced using inverse modelling of heat flow overlain on transect A-A' (with well paths and BCU displayed). (b) BCU in depth with 500 m interval contours shown. (c) RMS amplitude extraction of derived thermal conductivity at BCU. (d) Low case prediction of temperature along BCU. (e) Final temperature prediction using inverse modelled heat flow along BCU. Comparing with (d) some differences are apparent. Bulls eye like temperature anomalies in the north east are likely the translation of the interpolated heat flow (see Fig. 10a).

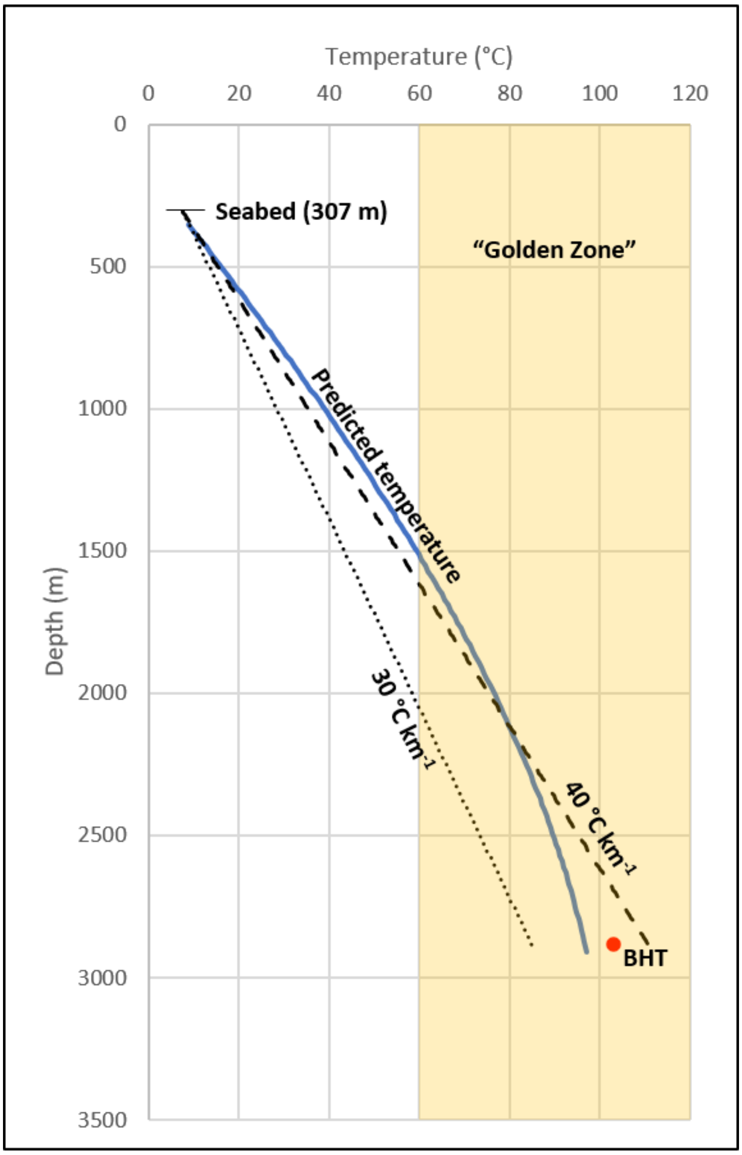

Figure 13: Modelled subsurface temperature at well 31/5-7 (Eos) (see Fig. 1) as part of the Northern Lights CCS project. "Golden zone" for sandstone reservoirs is also displayed for context. BHT displayed is from October 2020 Eos data release of preliminary results, indicating that prediction is in close agreement with what was discovered downhole (prediction is offset by 6 °C to reported BHT). Also shown are the temperature profiles taken from seabed assuming a constant linear geothermal gradient. Typically used geothermal gradients in basin modelling are 30 °C km^{-1} (dotted line) and 40 °C km^{-1} (dashed line). These are displayed to show how much subsurface temperature predictions may vary using standard processes, particularly at bottom hole (up to ±13 °C).

A.1 Appendix

Source	Geothermal gradient (°C/km)	Heat flow (mW m^{-2})

(Harper, 1971)	29.7	49.8 – 62.0
(Evans, 1977)		63
(Brigaud et al., 1992)	31.8 – 36.3	50 – 65
(Leadholm et al., 1985)	30 – 35	58.6 – 67
(Justwan et al., 2006)		52.3
(Cornford, 1998)		60 – 82
(Lucazeau & Le Douaran, 1985)		65
(Goff, 1983)	32	57 – 65
(Rüpke et al., 2008)	30 – 40	
(Ritter et al., 2004)		65

Table A.1: Some examples of reported geothermal gradient and heat flow for the NVG and surrounding basins from the literature.